Milestone Report

Absorber column CFD model validation against PNNL's device-scale absorber column on the LCFS unit

Work Performed Under

Activity Number 0004000.6.600.007.002 ARRA

Prepared by

Pacific Northwest National Laboratory

Richland, Washington 99352

Prepared for the

U.S. Department of Energy

National Energy Technology Laboratory

April 2020

Revision Log

Revision	Date	Revised By:	Description
1.0	2020.03.25	LANL team	Initial draft for data analysis
1.1	2020.03.31	Yucheng Fu	Initial draft for experiment and CFD modeling
1.2	2020.04.05	Zhijie Xu	Revision
2.0	2020.04.18	Yucheng Fu	Revision

Disclaimer

Acknowledgment of Funding

This project was funded under the Carbon Capture Simulation for Industry Impact ($CCSI^2$) under the following FWPs and contracts:

PNNL – 29828

Contents

List of Figures

List of Tables

Nomenclature

English

A_{cross}	Cross section plane area [m^2]
A_p	Ring surface area [m^2]
a_i	Interfacial area concentration [m^2/m^3]
a_p	Specific area [m^2/m^3]
d_h	Hydraulic diameter [m]
H	Absorber column height [m]
H_p	Packing height [m]
I_p	Particle moment of inertia [kg m^2]
F_c	Contact force in DEM model [N]
F_g	Gravity in DEM model [N]
F_σ	Surface tension force in momentum equation [N/m^3]
g	Gravity [m/s^2]
m_p	Particle mass [kg]
M_c	Moment acts on particle due to contact force [kg m^2/s^2]
n	Surface normal vector
p	Pressure [Pa]
Q	Flow rate [m^3/s]
T	Temperature [℃]
t	Time [s]
u_G	Gas superficial velocity in packed column [m/s]
u_L	Liquid superficial velocity in packed column [m/s]
V	Total occupied volume [m^3]
v_p	Particle velocity [m/s]

Greek Letter

α	Volume fraction of liquid [-]
ϵ	Packing Porosity [-]
θ	Contact angle [°]
κ	Curvature of local surface/interface [1/m]
μ_G	Viscosity of gas [Pa·s]
μ_L	Viscosity of liquid [Pa·s]
ρ_G	Density of gas [kg/m^3]
ρ_L	Density of liquid [kg/m^3]
σ	Surface tension [m/s]
ω_p	Particle angular velocity [1/s]
∇	Gradient operator [1/m]

SUBSCRIPT

abs	Absorber column
G	Gas
i	Interface
L	Liquid
norm	Normalized
reb	Reboiler

Acronyms

CA	Contact angle
$CCSI^2$	Carbon Capture Simulation for Industry Impact
CE	Capture efficiency
CFD	Computational fluid dynamics
CO_2	Carbon dioxide
CO_2BOL	CO_2 binding organic liquids
DEM	Discrete element method
DOCCSS	Discovery of Carbon Capture Substances and Systems
DoE	Design of experiments
FCM	Full-size column model
ID	Inner diameter
LCFS	Laboratory Continuous Flow System
OD	Outer diameter
PNNL	Pacific Northwest National Laboratory
RCM	Representative column model
SFR	Solvent flow rate
ST	Surface tension
V	Viscosity
VOF	Volume of fluid method

Absorber column CFD model validation against PNNL's device-scale absorber column on the LCFS unit

Yucheng Fu, Jie Bao, Chao Wang, Rajesh Kumar Singh, Dushyant Barpaga, Richard Zheng, Zhijie Xu
Pacific Northwest National Laboratory, Richland, WA 99352, USA

Sham Bhat, John Baca, Christine Anderson-Cook, James Gattiker
Los Alamos National Lab, Los Alamos, NM 87545, USA

Joshua Morgan
National Energy Technology Laboratory, Pittsburgh, PA 15236, USA

Executive Summary

Absorber column has been widely used for carbon dioxide (CO_2) capture in coal-fired power plants. High-fidelity computational fluid dynamics (CFD) models play an important role in absorber column design and solvents optimization, which help enhance the CO_2 capture efficiency and reduce the operation cost. This report provides a comprehensive description of the development of CFD absorber models at two different levels: the design and implementation of Pacific Northwest National Laboratory's (PNNL's) device-scale absorber column experiment and the methodology to combine the CFD results, experiment data, and Aspen model for a better understanding of the interface area in a packed column. A composite particle model is first proposed in the Discrete Element Method (DEM) packing process, which can model complex packing elements. This generates a realistic CFD column model. The obtained porosity ϵ and specific area a_p are comparable to the measured values of the Laboratory Continuous Flow System (LCFS) absorber column. Two levels of CFD absorber models were developed, namely the full-size column model (FCM) to simulate the entire packed column with a focus on the wall/entrance effects and the representative column model (RCM) to simulate a section of the column with a focus on the sensitivity study of interface area. A Design of Experiment (DoE) plan was developed to guide the collection of 100-run CFD data and 12-run experiment data. The 100 CFD runs were carried out in the RCM with Pro-Pak elements and cover a wide operation range and solvent properties. The impact of influential factors on the interface area in the packed column was investigated in detail. The CFD interface area was then combined with the experimental data and the Aspen model to infer some information of the effective contact angle in the column. The accuracy and uncertainties in the interface area and contact angle were quantified.

1 Introduction

The packed columns are frequently used in the solvent-based CO_2 capture tasks. In the packed column, countercurrent flow is generated by directing the solvent upside down while the flue gas is driven upward from the column bottom. In this process, the random or structured packing can spread the solvent as thin liquid films and droplets to increase the liquid-gas interfacial area for enhanced CO_2 capture efficiency. Dependent on the solvent selection and operation conditions, the packed column can be designed to provide a wide operation range and relatively low-pressure drop.

Multiple parameters can affect the performance of a packed column for CO_2 capture. In terms of the solvent property, the liquid viscosity μ_L, surface tension σ, and contact angle θ can vary dramatically among different types of solvents. These properties can relate to operation conditions and packing materials. In addition, the solvent/gas flow rates also have a direct influence on the packed column performance. Extensive experimental studies have been carried out to investigate the effect of these parameters. Considering the complexity of the problem, these factors had been explored by different works with various columns setup and solvents. The understanding of these parameter influences on the packed column performance can be biased with uncertainties from other coupled factors. For example, the contact angle can change with the variation of solvent surface tension and the packing material. It would be difficult to explore the contact angle effect only in the packed column without varying the surface tension or changing the packing material.

To address these potential issues and speed up the column/solvent design innovation, high-fidelity CFD absorber column models were developed in this report. Five key parameters—the liquid superficial velocity u_L, the gas superficial velocity u_G, the solvent viscosity μ_L, surface tension σ, and contact angle θ—are identified as the input parameters for the hydrodynamic simulations. These parameters can be varied independently in the CFD model. Therefore, it would be suitable for the parametric study in column performance and interfacial area prediction.

To validate the developed CFD absorber column model, the Carbon Capture Simulation for Industry Impact ($CCSI^2$) team and the PNNL Discovery of Carbon Capture Substances and Systems (DOCCSS) team were coordinated to achieve this goal. The DOCCSS team developed an LCFS system, which is a device-scale absorber column with a size small enough to be reproduced by the CFD model at a 1:1 scale. With this platform, the CFD model can be validated from two parts: 1) the accuracy of generating various types of random packed columns, which is highly relevant to the packed column performance; and 2) the interface area prediction from CFD hydrodynamic simulations. The second part includes two tasks. The

first task is to demonstrate that the CFD model can faithfully predict the full-size absorber column entrance effect and boundary influence on the solvent distribution. The second task is to explore the accuracy and uncertainties in predicting the interface area with various solvent properties and operating conditions. This is achieved by linking the CFD model, experiments, and Aspen model through the DoE method.

2 The LCFS Experimental Facility

This section describes the details of the experimental facility and setup used in this report. All experiments were performed at the PNNL's LCFS. This platform was the primary test platform for DOCCSS solvent (EEMPA) innovation and is small enough (2.5L solvent inventory) that key operating parameters can be easily changed. Further, the absorber for the LCFS has a right scale that can be modeled via CFD simulations compared to the pilot or commercial-scale columns.

2.1 Experimental Setup and Operation Range

The process diagram of the LCFS unit is illustrated in Fig. 2.1. The absorber column has an inner diameter of *ID* = 3'' and a height of *H* = 21''. The transparent acrylic wall is favorable for the visualization of the packing element and flow hydrodynamics. A water bath jacket is used to control the absorber temperature in the operation. It can maintain the absorber temperature in a range between 30°C to 60°C. The current operating upper limit of the absorber column is 4 psig imposed by the installed relief valves. With the *ID* = 3'', the packing element size (around 0.25'') is generally smaller than the commercial packing size used in the pilot- or industry-scale column.

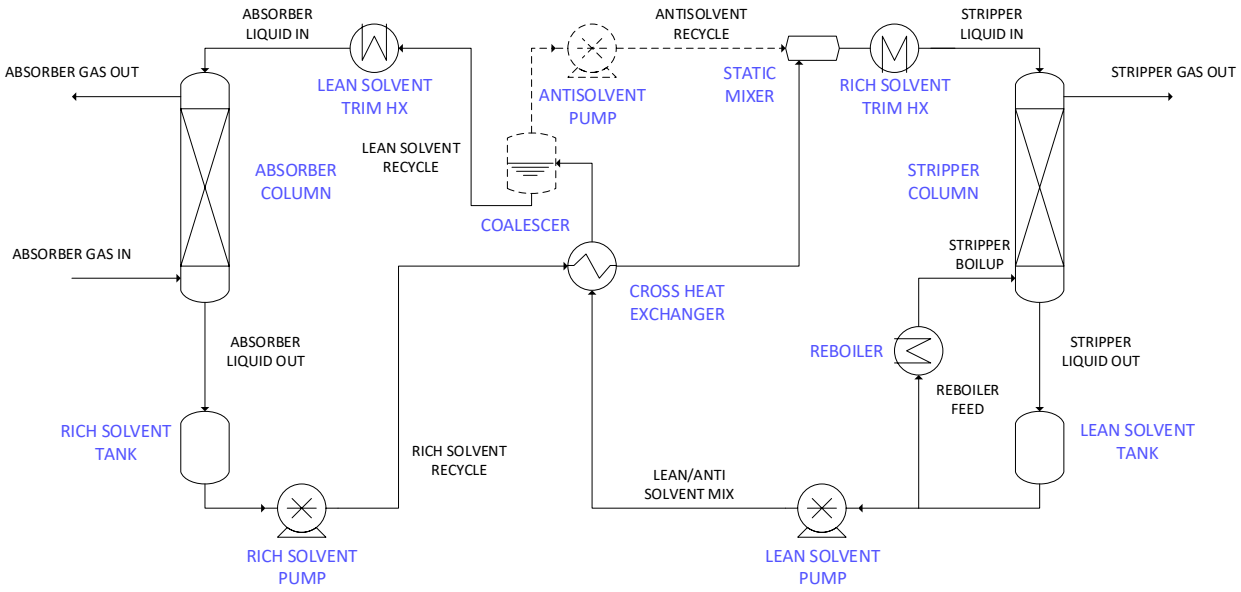

Fig. 2.1 The process diagram of the LCFS.

In the CO_2 absorption application, the column is operated in a countercurrent flow setting. The flue gas is injected from the bottom of the column and flowing upward. Two gas mass flow controllers are installed to regulate the N_2 and CO_2 flow rates from the gas cylinders, respectively. The N_2 can be delivered up to 200 SLM and the CO_2 can be delivered up to 23 SLM. The maximum turndown ratio of the system is 50:1 with a minimum gas flow rate of 5 SLM. In practice, the system is preferred to operate at 10 to 100 SLM of the total dry gas. The LCFS cart has the capability of humidifying the feed gas to 40°C dew point prior to the absorber column. With the EEMPA solvent studied in this report, the flue gas inlet moisture level is controlled to be less than 2–3 mol%.

The lean solvent is fed into the top of the absorber column and flows downward. The rich solvent exits at the bottom of the absorber column into a storage tank. A stripper column (reboiler) is equipped to separate the CO_2 from the rich EEMPA solvent. The processed lean solvent is then recirculated back to the absorber column. This enables the LCFS system to run continuously with a relatively small amount of solvent inventory. The stripper column is packed randomly with 0.24” Pro-Pak rings. The stripper can be operated with a temperature upper limit of 135 psig and a pressure upper limit of 30 psig.

The lean and rich solvent pumps are identical to the LCFS cart. The upper bound for the flow rate is 1.8 L/min. The smallest controllable flow rate is 0.1 L/min. At the high end of the flow, the gear pumps may exceed maximal rated differential pressure (torque limited), especially when the viscosity of the rich solvent is high. The preferred flow range is between 0.1 and 0.9 L/min. The stripper’s reboiler is a shell and tube exchanger (Exergy LLC, 00256-02) with forced circulation. The maximum shell side (heat transfer oil) temperature is 150°C. The boil-up flow rate can be controlled between 0.05 to 0.3 L/min. The rich-lean cross heat exchanger installed is a brazed-plate exchanger (Lytron, LL820G14). Additional trim heat exchangers are also installed in various locations to improve the system heating ability.

2.2 Absorber Column

In the LCFS cart, the absorber column is the main interest of the study. The CFD absorber model is built according to the design of the experiment absorber column. The details of the absorber column are shown in Fig. 2.2. In this picture, the column is filled with Pro-Pak packing for running all the experiments. Depending on the need, the absorber column can be taken out and filled with different types of random packing elements to study the effect of packing. Since the absorber column has a relatively small diameter of 3”, a small-size packing element with dimensions around 0.25” was selected for the study. At the shakedown tests, the column top is installed with a single injection tube at the center. The solvent maldistribution is observed when running the experiment. To better distribute the solvent, a 3D-printed

liquid distributor is then installed on the top of the column, as shown in Figure 2.2. The distributor has an orifice channel design with 12 drip tubes. On each drip tube, there are five orifices to improve the turndown ratio. The distributor is designed to have a flow rate from 0.1 to 0.5 L/min with 0.03”-diameter orifices. The Nylon is used for the 3D printing, which is tested and shown to be chemically compatible with the CO_2 binding organic liquids (CO_2BOL) family solvents.

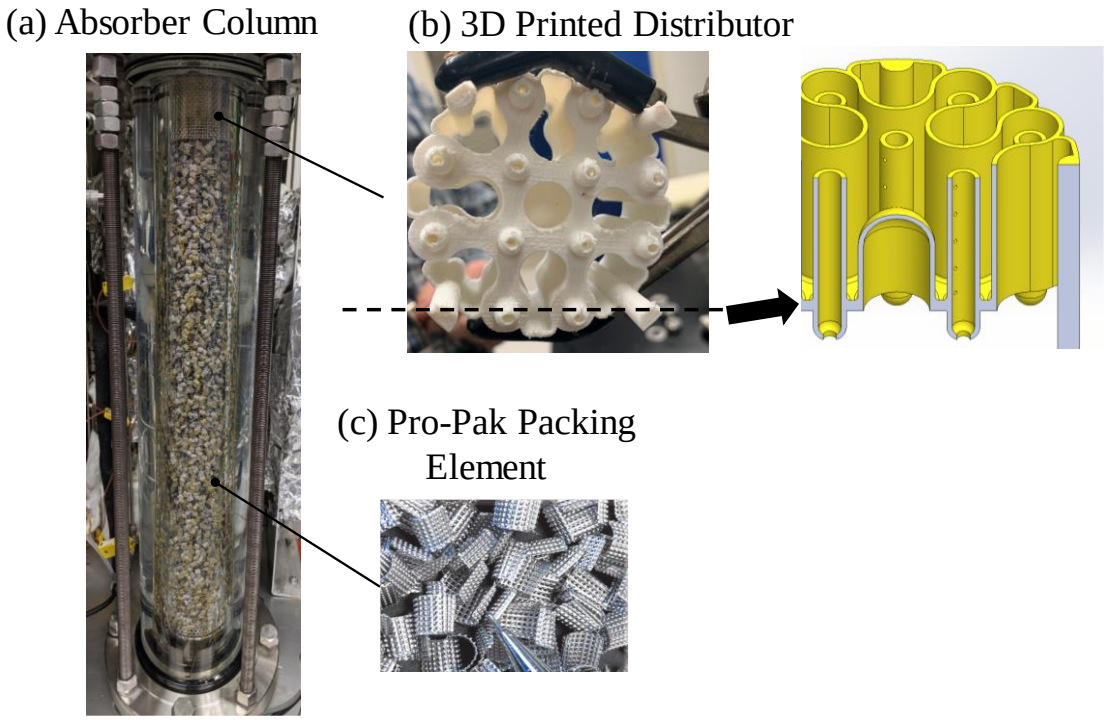

Fig. 2.2 The setup of the absorber column in the LCFS cart. The 3D-printed distributor is installed on the top of the column. The Pro-Pak is randomly dumped into the column in this snapshot.

2.3 Adjustable Parameters and Measurement

Factors that affect the performance of the absorber column are very complicated. Four critical parameters that can affect the absorber column efficiency in CO_2 capture are selected as the input parameters for the DoE and CFD model validation. These parameters are solvent flow rate Q_L, gas flow rate Q_G, reboiler temperature T_{reb}, and absorber temperature T_{abs}.

To calculate the CO_2 capture efficiency, the CO_2 at the top of the column is measured by CO_2 sensors. As mentioned in Section 2.1, the gas composition at the bottom can be controlled directly by mass flow controllers with given CO_2 mole fraction. The liquid compositions (CO_2 and H_2O) are analyzed offline by

the gas chromatography-mass spectrometry. For the solvent viscosity and surface tension parameters calculation, the developed Aspen EEMPA thermal package is used.

3 CFD Modeling of the Absorber Column

The development of the CFD full-size column model (FCM) and the representative column model (RCM are discussed in this chapter. The FCM was built with a 1:1 ratio compared to the absorber column in the LCFS cart. The full-scale model faithfully reflects the geometry, dimension, and the setup of the absorber column. The biggest advantage for the FCM is to investigate the boundary/wall and entrance effects on the solvent distribution, the factors causing the solvent maldistribution, and carbon capture performance. The acquired data will provide insights and facilitate column design and optimization.

On the other hand, an RCM was built with a size around one-tenth of the full-scale model. This model is more computationally affordable for parametric studies with hundreds of CFD simulation runs. The effects of solvent property and liquid/gas flow rate on the absorber column can be investigated using the representative-scale column.

In the following sections, the algorithms and related governing equations used for solving the countercurrent flow are introduced. A composite particle model is proposed in the DEM process for generating a realistic random packed column. The setup and details of FCM and RCM are then discussed, respectively.

3.1 Mathematical Formulations

The 3D multiphase flow in random packed column is simulated using commercial CFD software: STAR-CCM+[1]. The volume of fluid method[2] is used to track the gas-liquid interface of the liquid film, droplet, and freestream that appeared in the countercurrent flow. With the volume of fluid method, the mass and momentum conservation equations can be solved with a single equation. The mass conservation equation has the form of:

$$\frac{\partial \rho}{\partial t} + \nabla \cdot \left(\rho \mathbf{u} \right) = 0, \tag{3.1}$$

and the momentum equation has the form of:

$$\frac{\partial \rho \mathbf{u}}{\partial t} + \nabla \cdot \left(\rho \mathbf{u}\mathbf{u} \right) = -\nabla p + \mu \nabla^2 \mathbf{u} + \rho \mathbf{g} + \mathbf{F}_{\boldsymbol{\sigma}}, \tag{3.2}$$

where ρ is density, μ is viscosity, p is pressure, and $\mathbf{F}_{\boldsymbol{\sigma}}$ is the surface tension force at the liquid-gas interface. The ρ and μ are weighted by the fraction of liquid and gas in the computational cells

$$\rho = \rho_L \alpha + \rho_G \left(1-\alpha\right), \tag{3.3}$$

$$\mu = \mu_L \alpha + \mu_G \left(1-\alpha\right), \tag{3.4}$$

where α is the void fraction of the liquid phase. The interfacial surface tension force $\mathbf{F_\sigma}$ is modeled with the continuum surface force approach as [3]:

$$\mathbf{F_\sigma} = \sigma\kappa\mathbf{n}\,, \tag{3.5}$$

where σ is the surface tension coefficient, κ is the local surface mean curvature, and $\mathbf{n}$ is surface normal vector. The κ and $\mathbf{n}$ are calculated as:

$$\mathbf{n} = \nabla\alpha\,, \tag{3.6}$$

$$\kappa = -\nabla\cdot\hat{\mathbf{n}} = -\nabla\cdot\frac{\nabla\alpha}{\left|\nabla\alpha\right|}\,. \tag{3.7}$$

On the wall region, the unit surface normal $\hat{\mathbf{n}}$ is enforced as $\hat{\mathbf{n}}_\mathbf{w} cos\theta + \hat{\mathbf{t}}_\mathbf{w} sin\theta$, where $\hat{\mathbf{n}}_\mathbf{w}$and $\hat{\mathbf{t}}_\mathbf{w}$ are the unit normal and tangential vectors on the wall surface, respectively. The contact angle θ is where the gas-liquid interface meets the solid surface.

The transport of the void fraction α is governed by:

$$\frac{\partial\alpha}{\partial t} + \nabla\cdot\left(\mathbf{u}\alpha\right) = 0. \tag{3.8}$$

Solving the transport equation, the volume fraction of the liquid phase can be obtained in each computing cell. The gas-phase volume fraction can be easily calculated as 1-α. To acquire a sharp and immiscible interface, the high-resolution interface capturing scheme [4] is used for the discretization of convection terms to reduce the numerical diffusion.

The simulations in this study were run on the PNNL Institutional Computing high-performance cluster. Depending on the scale of the problems, 5 to 40 computing nodes will be used for running the CFD model. Each computing node has dual Intel Haswell E5-2670 CPUs giving 24 cores per node.

3.2 Column Packing with DEM Method and Composite Particle Model

In the actual experiment, the packing elements are dumped into the absorber column by removing the liquid distributor. The DEM is used to model the random packing process. This ensures the generated packing has a realistic packing element distribution, which is closely related to the countercurrent flow

hydrodynamics. Three types of random packing elements: Raschig ring, Pro-Pak, and Pall ring are selected for generating the absorber column model. The dimensions of the three packing elements are shown in Fig. 3.1. The Raschig ring has an outer diameter of *OD* = 6 mm and a height of *H* = 6 mm. The wall thickness of the Raschig ring is about 0.8 mm. The Pro-Pak has a half-cylinder shape with small straight extension to non-curved edges. It has a diameter of *OD* = 6.1 mm and a height of *H* = 6.1 mm. The metal sheet has a thickness of 0.0762 mm. The Pro-Pak packing has small perforations on the surface with a hole density of 159/cm^2. The perforations can reduce the packing pressure drop and increase the ring occupied space. The Pall ring geometry is adapted from Chen et al. [5]. It has a *OD* = 16 mm and *H* = 16 mm. The wall thickness is 0.5 mm.

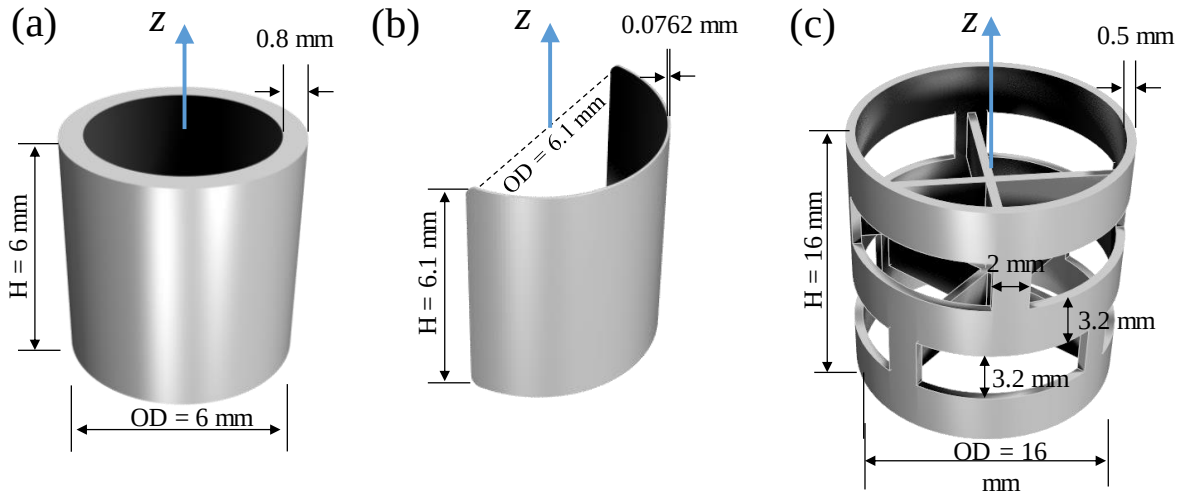

Fig. 3.1 The dimensions of three random packing elements, (a) Raschig ring, (b) Pro-Pak, and (c) Pall ring, used in the CFD simulations.

In the DEM method, the movement of those particles are governed by contact force F_c, gravity F_g, and friction forces as [6]:

$$m_p \frac{dv_p}{dt} = F_c + F_g, \tag{3.9}$$

$$I_p \frac{d\omega_p}{dt} = M_c, \tag{3.10}$$

where m_p and v_p are the particle mass and velocity, respectively. I_p is the particle moment of inertia. The ω_p term stands for the particle angular velocity, and M_c is the moment which acts on an individual particle due to contact force, which in turn acts on the particle at a point other than the particle center of gravity. In the

DEM method, disc, sphere, and cylinder particles are commonly used to represent the simulated object due to their relatively simple geometry. With the recent development of the DEM method, the super-quadrics, super ellipsoids, and composite particle-based models [7]–[10] are developed to approximate the non-regular shape objects. In the composite particle method, it combines multiple spherical particles as a rigid super-object, which is unbreakable. Considering the dramatically different and non-regular shape of the packing elements, the composite particle model is more suitable to model the interactions among these complex pacing elements and create a realistic packing pattern. To ensure the accuracy of the model, the arrangement of spheres in the composite particle model is designed manually, as shown in Fig. 3.2. The Raschig ring composite model is generated by piling up eight layers of sphere rings. Each sphere has a diameter of 0.82 mm. The sphere diameter is determined based on the Raschig ring wall thickness and was enlarged by 2.5%. The red spheres in the figure highlight the refined edged on the top and bottom of the Raschig ring. These two treatments reduce the possibility of inter-penetration of the particles in contact. A total of 210 spheres are used for compositing the Raschig ring. The Pall ring packing follows the same strategy since it has a similar shell shape and the interior structure with a negligible impact on the packing process, compared with the Raschig rings. The Pro-Pak composite model is shown in Fig. 3.2 (b). The green spheres are arranged in a half-cylinder shell shape to represent the metal sheet body of the Pro-Pak. It has the same dimensions as the Pro-Pak used in the experiment. The edge of the metal sheet is refined to prevent the packing element penetration when composite particles are in contact during the packing process. Another layer of red spheres is attached to the half-cylinder shell to represent the perforations on the Pro-Pak. This ensures the packing density and pattern can be correctly reproduced in the DEM. With this setup, a total of 1314 small spheres are required for a Pro-Pak composite model.

(a) Composite model: Raschig ring

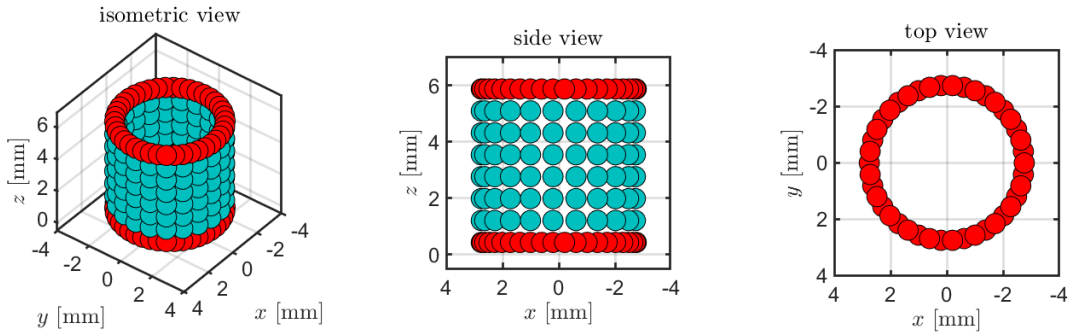

(b) Composite model: Pro-Pak

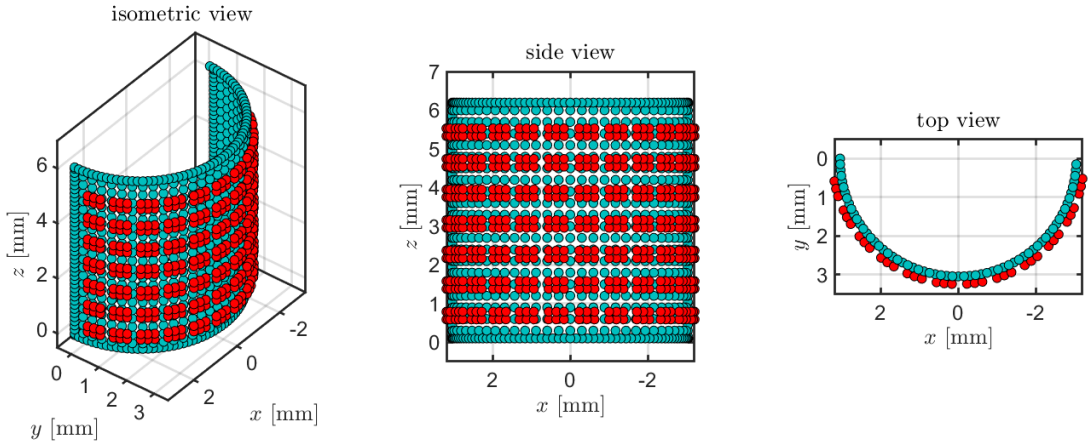

Fig. 3.2 The composite model design of (a) Raschig ring and (b) Pro-Pak used in the DEM for the column packing process. The red particles in Raschig ring models highlight the refined region in the top and bottom. The red particles in the Pro-Pak highlight the protruding part arisen from packing element perforation.

After all the composite particles filled the cylindrical container and settled down, the position and orientation vector of each composite particle is exported. The actual packing geometry as shown in Fig. 3.1 is used to replace the settled composite particles. By subtracting these packing elements from the absorber column, the computational domain can be acquired for the further hydrodynamics study. Considering the relatively small effect of flow on the packing arrangement, all the rings are treated as still during the countercurrent flow simulations. A comparison of the CFD-generated packing with experimental packing is shown in Fig. 3.3. It was found that the DEM-generated Raschig ring packing has a similar random pattern as observed in the real packing. The Raschig ring settled down in both parallel and perpendicular

directions to the column wall. An exploded view of the packing is shown in Fig. 3.3 (c). This image shows the advantage of using the composite model compared to the simple cylinder representation for the Raschig rings. With a plain cylinder model, the cylinder edge can only contact the top and bottom surface of other rings. The packing density generated from the cylinder model is expected to be slightly lower than the acquired in the experiment. With the composite particle model, the hollow Raschig ring shape can be modeled accurately and the edge of the Raschig ring can be partially pushed into the hollow center region of other Raschig rings.

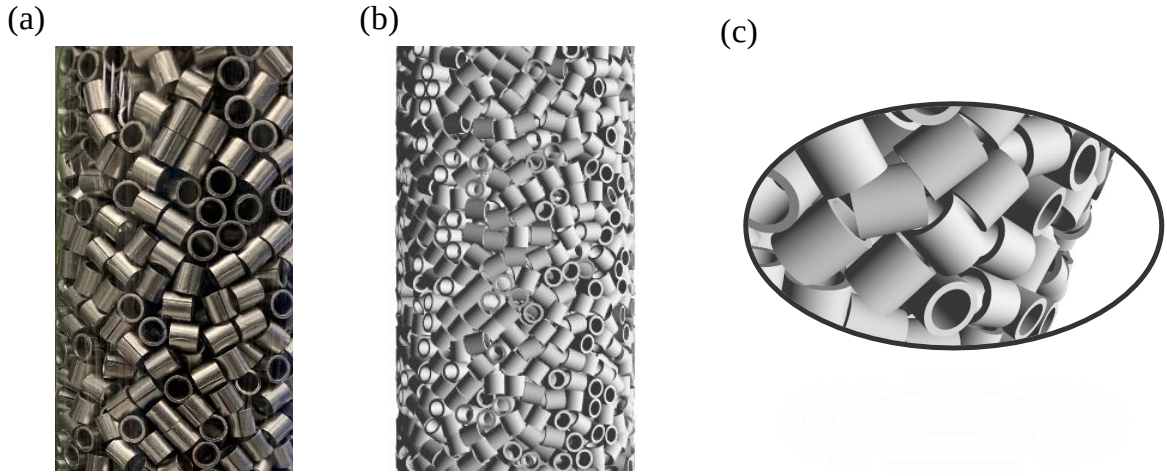

Fig. 3.3 Comparison of Raschig packing patterns in the (a) experiment absorber column and (b) in the CFD model. The composite Raschig particle is used in DEM for CFD packing. (c) An exploded view of the CFD packing.

The ring distribution is compared in Fig. 3.4 using both the cylinder and composite particle model. The Fig. 3.4 (a) shows the ring density distribution along the column flow directions. With the cylinder model, the ring density is not uniform across the column height. The bottom rings are more compacted than the ring on the top. One possible reason is that the cylinder model has smaller friction compared to real Raschig rings. In real packing, the edge of the Raschig ring can be partially inside the hollow region of another ring, which creates additional friction to stabilize the packing position. In the cylinder model, one edge can only contact the surface of another cylinder, which significantly reduces the friction. With increasing pressure by adding more rings, the cylinder model packing will be condensed at the bottom but with less packing elements on the top. Using the composite particle model instead, the ring contacts can be modeled correctly, and the generated packing has a much more uniform distribution along with the entire height of the column. The Fig. 3.4 (b) shows the packed ring distribution at the cross section plane. Both

the cylinder and composite particle model show a similar distribution since the gravity force does not act on the horizontal direction.

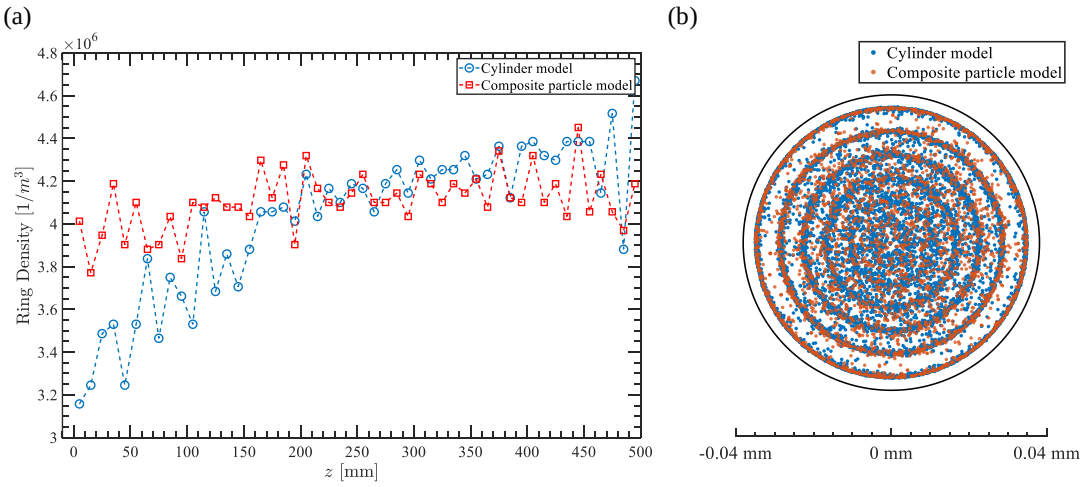

Fig. 3.4 Comparison of Raschig ring distribution in the absorber column using the cylinder and composite particle model. (a) Ring counts along the vertical direction; (b) Raschig ring distribution across the plane.

The generated packed column specific area is also compared with the experiment and specification sheets for validation. The comparison results are shown in Table 3.1. For the Raschig ring and Pro-Pak ring, an *ID* = 7.62-cm-size column is used for packing. With the known packed ring locations and surface area after it has settled down, the specific area in the CFD modeling can be calculated directly by dividing the total ring surface area A_p with the corresponding occupied volume *V*. In the LCFS cart, all the dumped rings in the packed column will be weighed after finishing the packing. With known averaged single packing element weight, the total packing surface area and specific area can be calculated accordingly. With a relatively small column diameter *ID* = 7.62 cm, the actual experiment-acquired specific area is smaller than the one given by the specification sheet due to the wall effect. From Table 3.1, it can be seen that both the Raschig ring and Pro-Pak packing generated by the DEM process can predict the specific area with an uncertainty smaller than 5%. For the 16-mm Pall ring, a much larger column (*ID* = 0.27 m, *H* = 0.26 m) is packed for validation and the specific area is calculated at the column center region. This helps to keep the wall effect to a minimum and make the specific area calculation method comparable to the specification sheet. The simulated specific area (308 m^2/m^3) shows a reasonable match with the specification sheet results of 303 m^2/m^3.

Table 3.1 Comparison of CFD packing using the composite particle model with experiment or specification sheet packing data.

Packing Type	CFD Packing		Benchmark Packing	
	Specific area a_p [m^2/m^3]	Remark	Specific area a_p [m^2/m^3]	Remark
Raschig Ring (6 mm)	857.5	Same packing geometry with experiment.	817.8	Experiment packing data with column *ID* = 0.0762 m.
Pro-Pak (6 mm)	939.5	Same packing geometry with experiment.	962.4	Experiment packing data with column *ID* = 0.0762 m.
Pall Ring (16 mm)	308.0	Rings Packed in a large column of *ID* = 0.27 m and *H* = 0.26 m. Specific area sampled at column center.	330.0	Specification sheet data. No wall effect.

3.3 Full-scale Column Model

Fig. 3.5 shows the comparison of the absorber column used in the LCFS cart and in the CFD simulations. The CFD model has a 1:1 scale ratio compared to the column used in the experiment. The solvent is injected at the top of the column. The schematic is shown in Fig. 3.5 (c) with a single tube injection design, which is initially used in the experiment. Later, a distributor is installed on the top of the column to reduce the solvent maldistribution near to the entrance. The CFD model is also revised to reflect this modification.

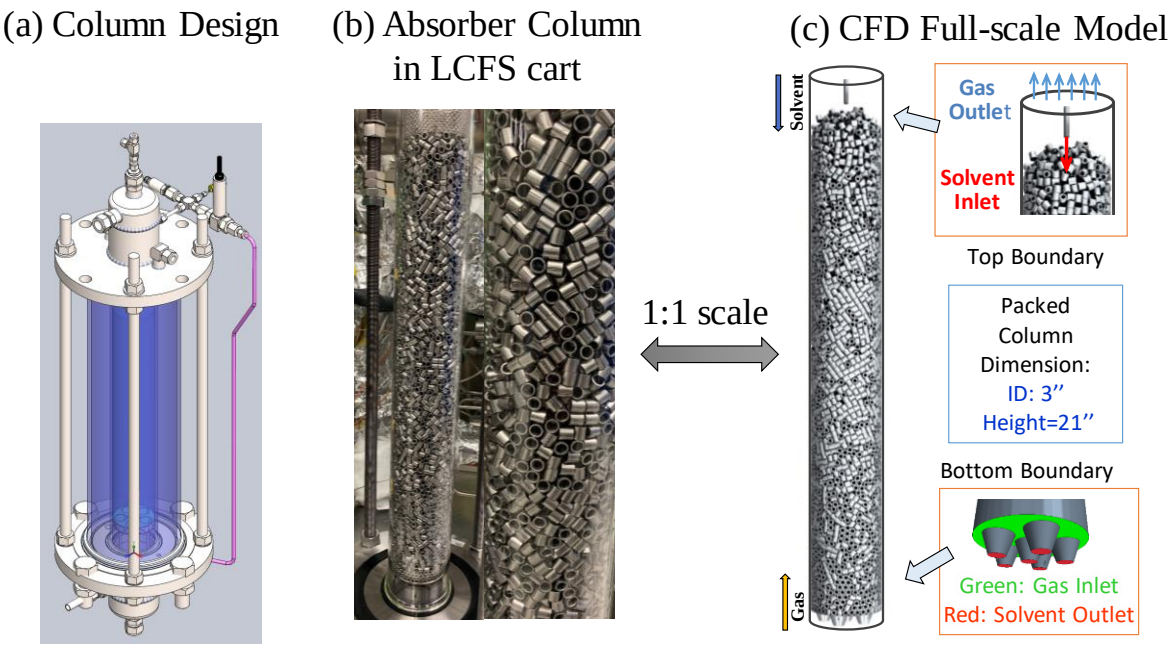

Fig. 3.5 (a) CAD file showing the design of the absorber column; (b) the absorber column used in the LCFS cart packed with Raschig rings; (c) the full-scale CFD model packed and the boundary condition setup for simulations.

To demonstrate the capability of the full-scale CFD model, simulations were first run with a single injection tube setup. The EEMPA solvent is used in the simulation with a flow rate of Q_L = 0.76 L/min. A qualitative comparison between the CFD simulation results and the experiment is shown in Fig. 3.6. In the experiment, the solvent is dyed with blue dye for visualization. With a single tube injection, the solvent shows a strong entrance effect before a uniform distribution in the column. This was observed from both simulations and experiments, where the dyed solvent shows a pyramid shape near to the entrance. The cross section data acquired in the CFD simulation shows a similar pattern at the entrance region. The plot shows the normalized interfacial area concentration development along the flow direction both with and without a distributor. With a single injection tube, the solvent takes around 0.125 m (about one-fourth of the column height) before uniformly being distributed in the column. After the installation of the distributor, the entrance effect is shortened by around 10 cm. After around 0.02 m traveling distance, the solvent is already distributed uniformly in the column. Therefore, distribution design does significantly improve the solvent distribution in the packed column.

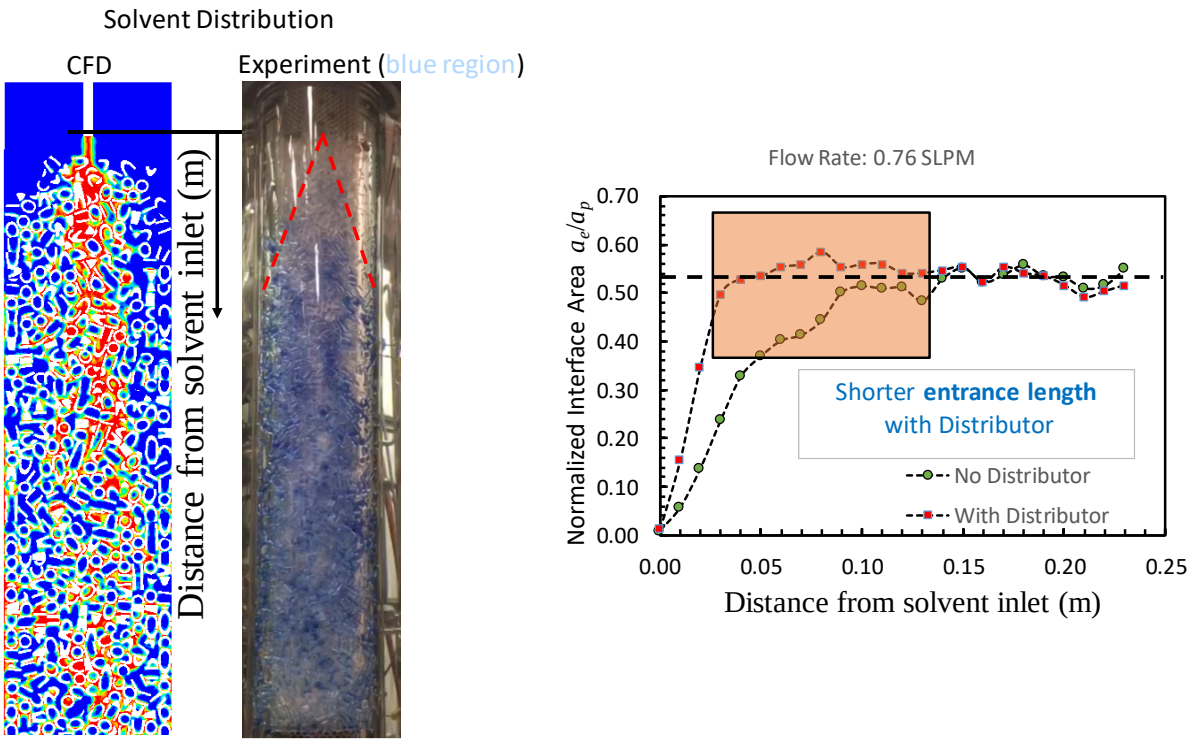

Fig. 3.6 Column entrance effect and mitigation with the 3D-printed distributor.

3.4 Representative Column Model

As shown in the full-scale CFD column model, the solvent distribution becomes relatively uniform along the flow directions except for the region near the entrance. With this observation, it would be reasonable to simulate a small section of the column to study the absorber column performance. This helps to reduce the computational cost and carry out the parametric study more efficiently. To avoid the solvent maldistribution caused by the entrance effect, the distributor is installed for all the RCM. Three types of representative columns are built for Raschig rings, Pro-Pak, and Pall rings, respectively.

3.4.1 Characteristics of the Random Packed Column

The generated RCMs are presented in Fig. 3.7. The packing distribution is acquired from the center region of a large packed column. This removes the non-uniform distribution of the packing element in the top regions of large column and can better model the solvent flow/distribution in the column. The whole computational domain height H_c is 6 cm for Raschig rings and Pro-Pak, and 12 cm for the Pall rings. The packed rings height H_p is 5 cm for Raschig rings and Pro-Pak and 10 cm for the Pall rings. Similar to the

full-scale column boundary setup, the solvent is injected at the top of the column through the uniformly distributed tubes marked in blue color. The rest of the top surface marked in red are the gas outlet regions. The bottom of the column has both outward solvent and inlet gas flow.

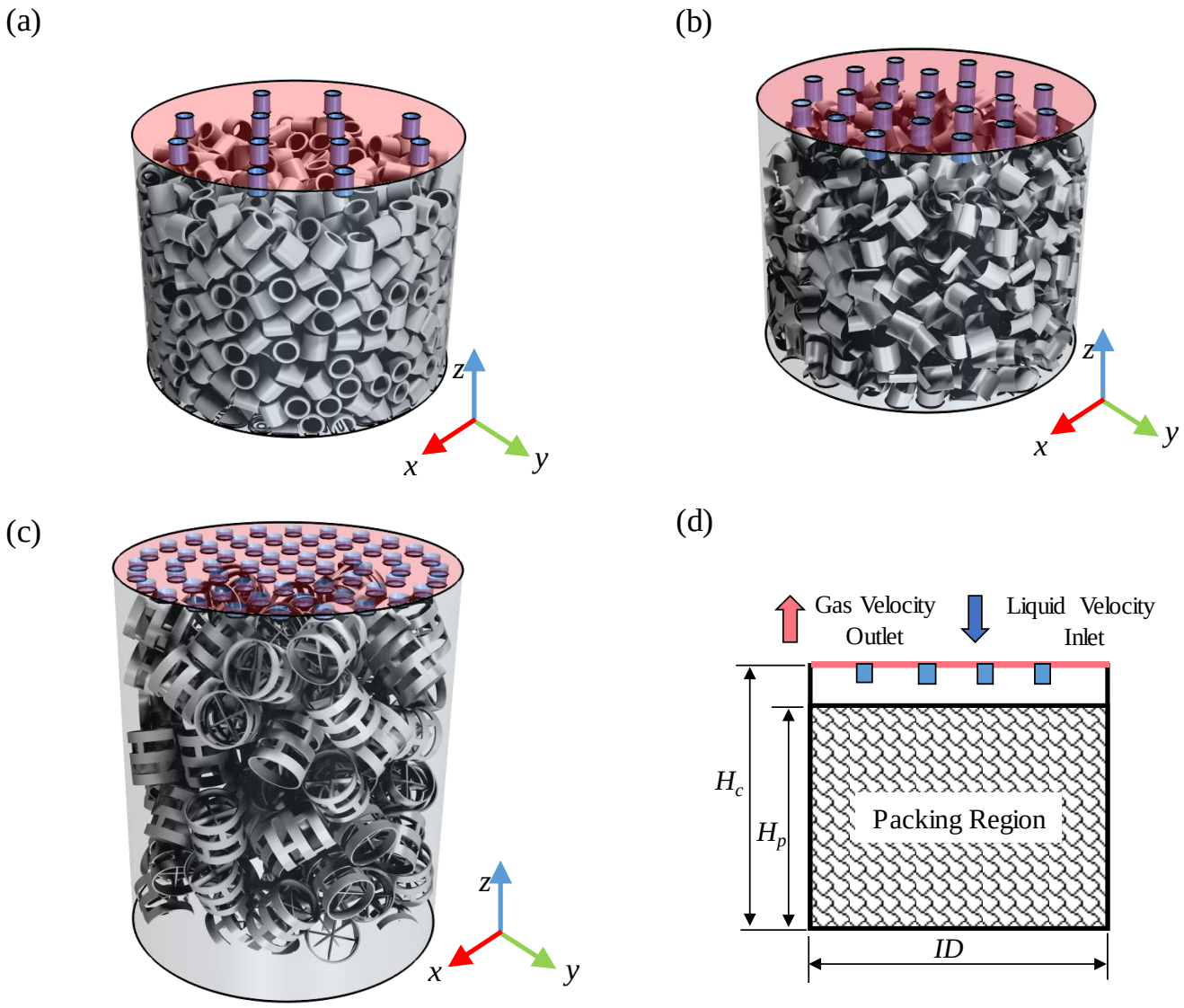

Fig. 3.7 Schematics of the RCMs packed with (a) Raschig rings, (b) Pro-Pak, and (c) Pall rings. (d) The dimension notation and the boundary conditions of the CFD RCMs.

The detailed information for the representative packed column is summarized in Table 3.2. Raschig ring and Pro-Pak has the same column diameter of 7.62 cm as the full-size column. The Pall ring has a larger size with a diameter of 16 mm. To ensure a reasonable column-to-ring diameter ratio, the Pall ring representative column has an inner diameter of 10 cm. Due to the large Pall ring size, the Pall ring packing has the smallest specific area of a_p = 209.1 m^2/m^3 among the three packed columns. The Raschig ring and Pro-Pak have a similar specific area of a_p = 857.5 m^2/m^3 and a_p = 939.5 m^2/m^3, respectively. With a thin wall, the Pro-Pak and Pall ring both have a porosity over 95%. The Raschig ring has a relatively small porosity of 68.4% due to its thick wall. The hydraulic diameter d_h is also provided for each representative column in the table, which is defined as:

$$d_h = \frac{4\varepsilon}{a_p}. \tag{3.11}$$

Table 3.2 Summary of the geometrical parameters of the developed representative column packed with Raschig rings, Pro-Pak, and Pall rings.

CFD Model	Geometry			Specific Area a_p [m^2/m^3]	Porosity ϵ [%]	Hydraulic Diameter d_h [mm]
	Column Height H_c [cm]	Packing Height H_p [cm]	ID [cm]			
(a) Raschig Ring Column	6	5	7.62	857.5	68.4	3.2
(b) Pro-Pak Column	6	5	7.62	939.5	96.8	4.1
(c) Pall Ring Column	12	10	10	209.1	97.4	18.6

Along with the column-wise parameters, the local ring distribution and packing characteristics are also important for the absorber column hydrodynamics. These details are shown in Fig. 3.8. Each dot in the plots represents a single ring mass center. The first row shows the packed ring locations at the cross section plane *x-y*. The Raschig ring shows the most noticeable organized annular patterns at near-wall regions. Moving toward the center, the ring location becomes more scattered and the circular shape is less distinct. The Pro-Pak is much denser compared to the Raschig ring due to its half-cylinder shape design. With the

nonsymmetrical shape, the Pro-Pak can contact the wall with its straight edge or the curved half-cylinder surface. This results in a more scattered ring center distribution and no obvious annular shape can be observed in the plot. The Pall ring has much less density due to its large size, and the distribution is sparser. The second row shows the orientations of these rings in the packed column. The orientation of the ring is defined as the angle between the ring main *z*-axis and the horizontal plane. All three rings show a decrease in trends of occurrence when the orientation angle increases. This indicates that a large portion of the rings lays nearly flat in the packed column. The rings that settled down in vertical direction are less stable compared to the horizontally settled particles. If looking at the rings in the different radial regions, it would found that the wall has a significant influence on the packing element orientation for the Raschig ring and Pall ring. In the near-center region ($0< r < R/3$), the distribution of the ring orientation is flattened compared to the ring orientations in the near-wall region ($2R/3<r<R$). For the Pro-Pak, the orientation shares a similar profile in three radial regions. This shows that the column wall has a less significant influence on the nonsymmetrical packing element orientation.

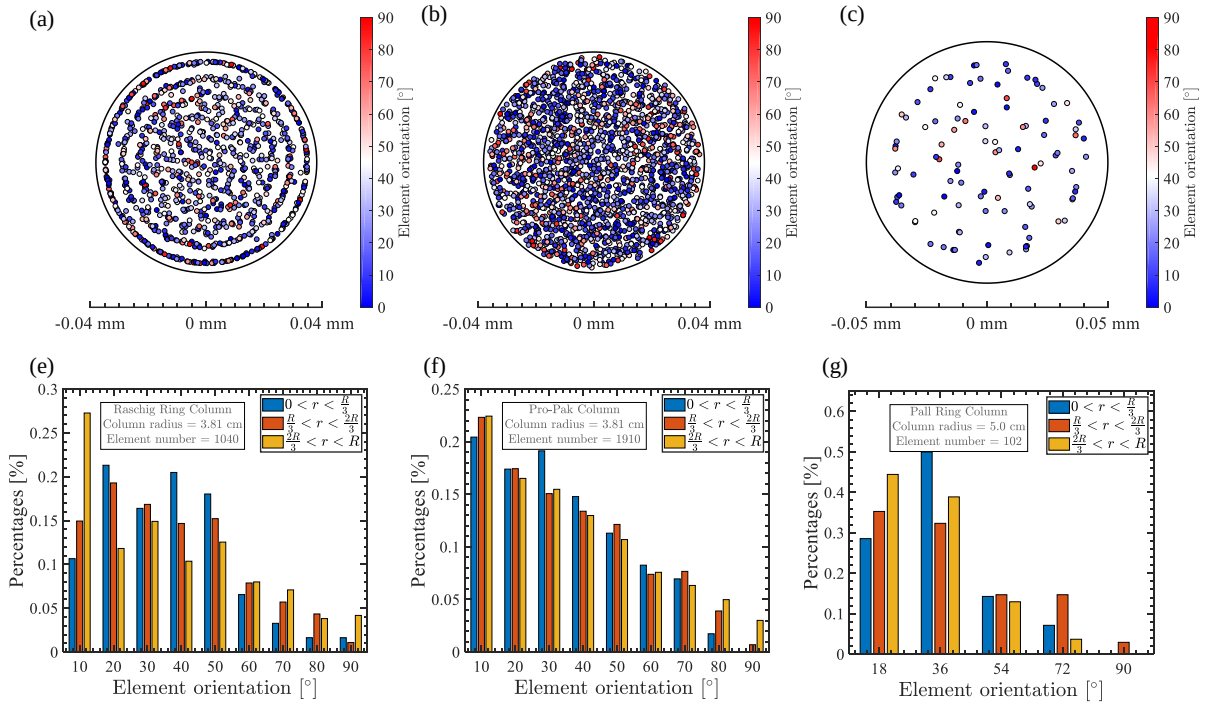

Fig. 3.8 First row: the distribution of (a) Raschig ring, (b) Pro-Pak, and (c) Pall rings at the cross section plane. Second row: the packing orientation comparison of (e) Raschig ring, (f) Pro-Pak, and (g) Pall rings at three different radial regions.

The porosity ϵ and specific area a_p are two important parameters in the packed column for pressure drop, mass transfer area, and liquid holdup prediction. The non-uniform distributions of the specific area

along the radial direction can affect the performance of the column and the countercurrent flow hydrodynamics [11]. The radial porosity and specific area distributions in representative columns are shown in Fig. 3.9. At the near column wall $r/R = 1$, the ring element edge has a tangential contact with the absorber column wall. This decreases the density of the ring near the wall and yields a porosity close to 1 and a specific area near 0 for all three types of packing. Moving toward the center region, periodic fluctuation of porosity and specific area a_p is observed, which is consistent with the ring distribution pattern as described in Fig. 3.8. The Pro-Pak curve is flattening out, because its distribution is more random and uniform. With more rings in a local region, the available surface area will increase and results in a larger specific area a_p. The porosity and a_p always shows the opposite trend.

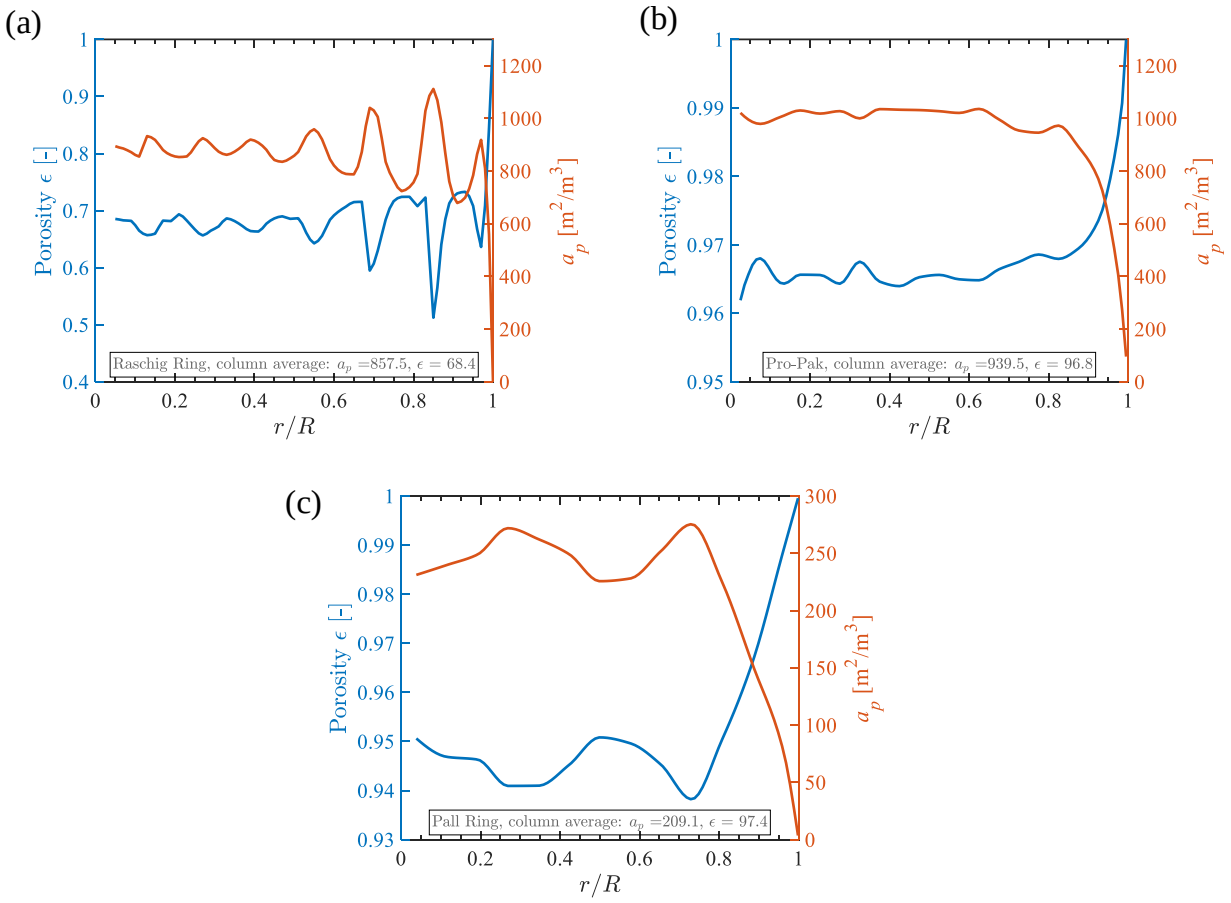

Fig. 3.9 Radial porosity and specific area distributions in the random packed column with (a) Raschig rings, (b) Pro-Pak rings, and (c) Pall rings.

3.4.2 Meshing and Convergence Study

A snapshot of generated mesh for a representative column is shown in Fig. 3.10. This column is packed with the Pro-Pak packing. The computational domain is created with polyhedral mesh, which is suitable and efficient for complex geometry. The prism layer is generated for all the solid surfaces, including the Pro-Pak surface and absorber column wall. This helps to solve the wall boundary layer film flow with higher accuracy.

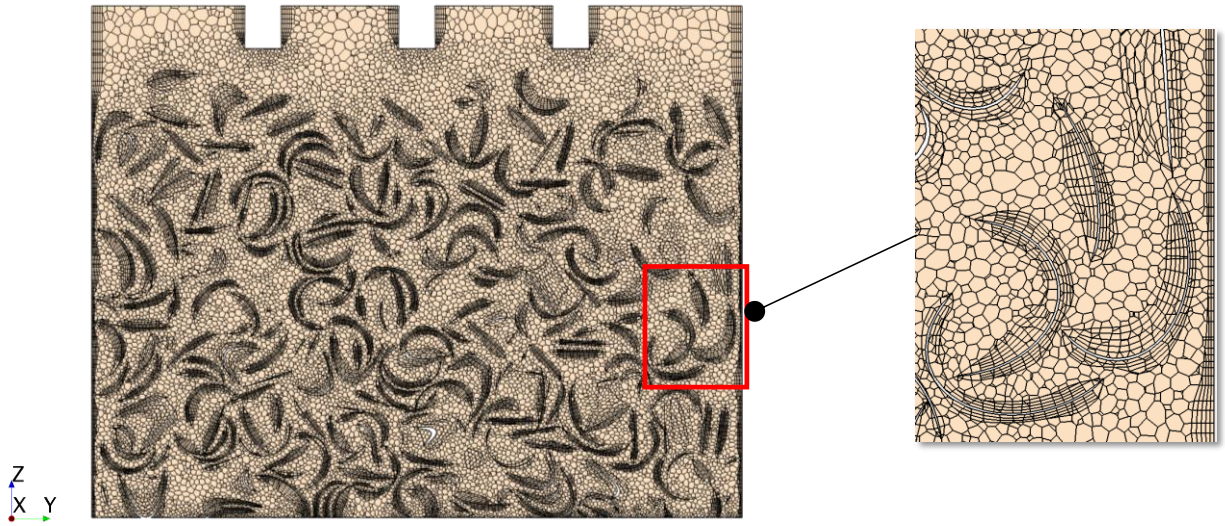

Fig. 3.10 Snapshot of the meshing used for the representative column CFD simulation with Pro-Pak rings. The visualized cross section cut through the column center vertically. The exploded view shows the prism layers generated near the ring and column wall surface.

A total of 5.8 million mesh elements is generated for the representative column with Pro-Pak rings for simulations. A convergence study is carried out to validate the mesh used is appropriate and accurate. Five different mesh grid resolutions are tested, and the results are shown in Fig. 3.11. This covers the mesh element number from 3 million to 8.5 million. The simulation is run with a flow rate of u_L = 0.0021 m/s and u_G = 0.2276 m/s. The surface tension is σ = 0.01 N/m and the viscosity is μ = 0.00745 Pa s. The contact angle θ is selected as 41°. Both the liquid holdup and interfacial area concentrations a_i are plotted. As can be seen in Figure 3.11, the solution converges with the mesh element number larger than 5.8 million. The difference for liquid holdup and interfacial area concentration are both smaller than 3% for 5.8 million meshing compared to the finest 8 million meshing setups.

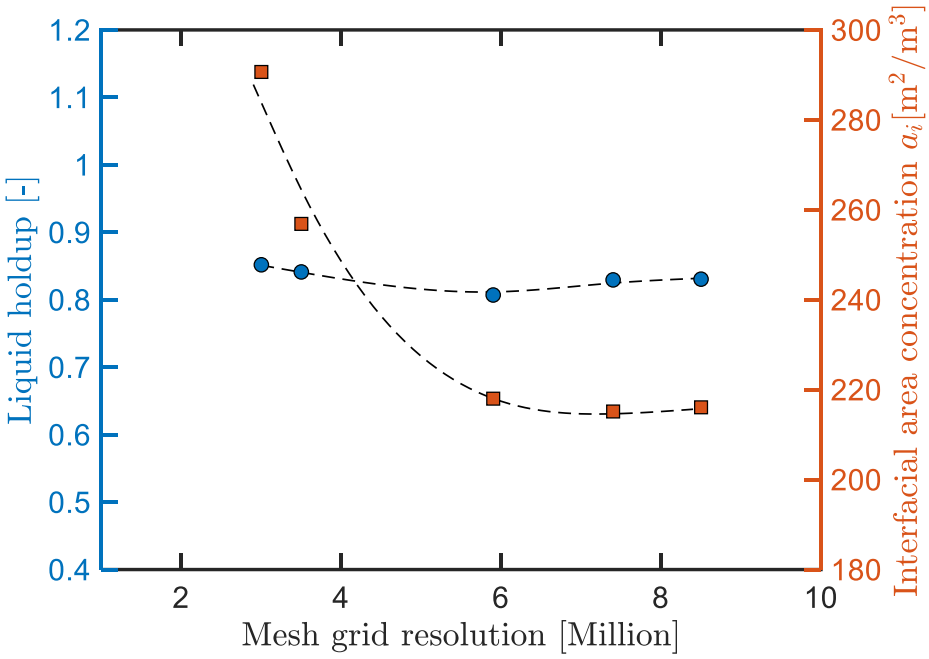

Fig. 3.11 Mesh grid convergence study with different resolutions. The liquid holdup h_L and interfacial area concentration a_i are plotted for comparison.

3.5 Sensitivity Study

A preliminary sensitivity studied had been carried out in this section. The influence of the contact angle θ, surface tension σ, and liquid viscosity μ_L in the interfacial area concentration a_i is investigated with a factorial design test. Four contact angle values ([10, 40, 60, 90]), two surface tension values ([0.0277, 0.0664] N/m) and three liquid viscosities values ([0.00246, 0.005, 0.01] Pa s) are selected for the tests. This results in a total of 24 cases. The solvent flow rate is kept at a constant of u_L = 0.00148 m/s and the gas velocity is set as zero. The results are plotted in Fig. 3.12. Note that these three physical properties are likely interrelated in reality, versus independent as modeled. Overall, the contact angle shows the most significant influence on the predicted a_i. Increasing the contact angle from 10 to 90, the a_i has decreased nearly 5 times from 540 m^2/m^3 to 110 m^2/m^3. Compared to the contact angle, the solvent viscosity and surface tension have much less influence on the liquid-gas interfacial area, even with a significant variation. These observations are consistent with the existing literature [12], [13]. To further investigate these parameters' influence, a more comprehensive DoE plan was carried out in the next chapter to cover a wider parameter space and response range.

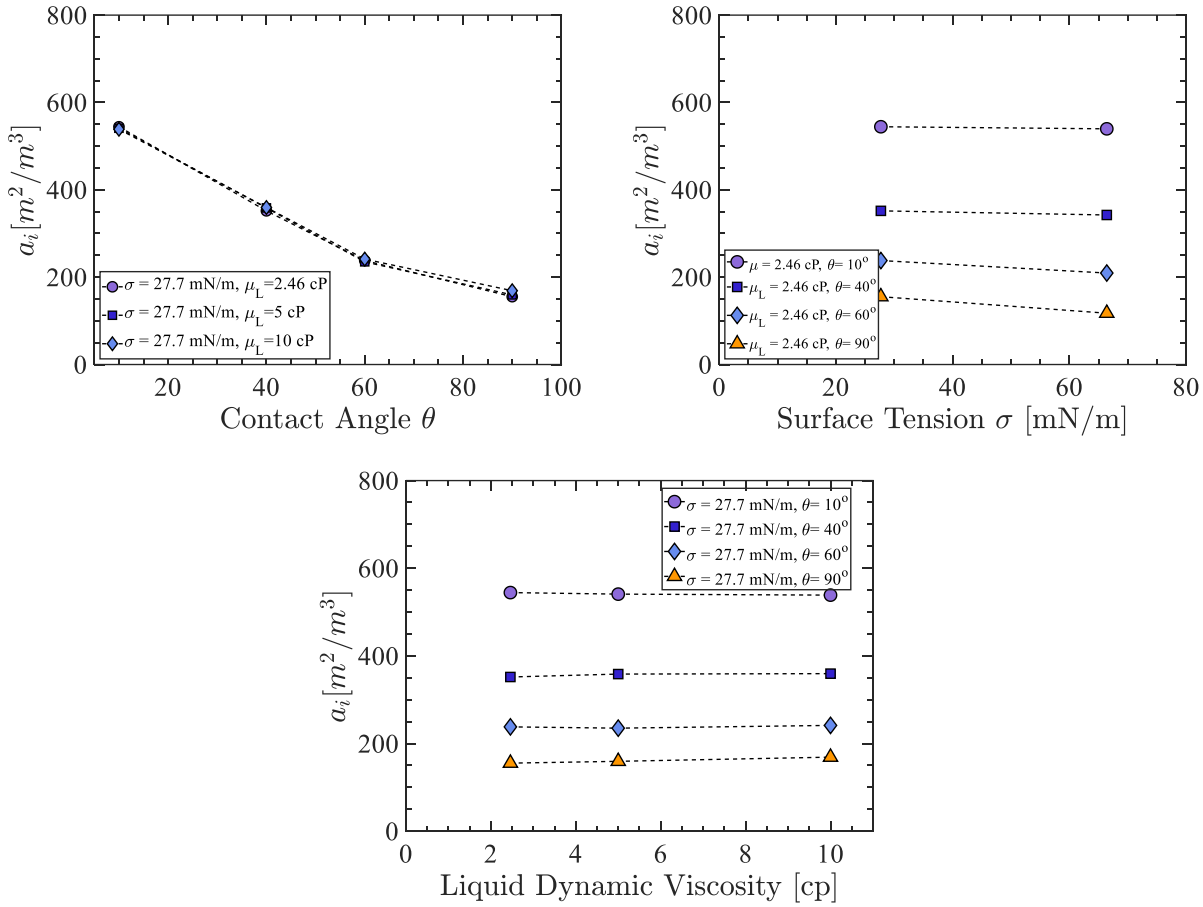

Fig. 3.12 Sensitivity study of the contact angle θ, surface tension σ and solvent viscosity μ_L influence on the interfacial area concentration a_i. The CFD RCM with Raschig rings is used here with u_L = 0.00148 m/s and u_G = 0 m/s

4 Design of Experiment

This chapter aims to propose a DoE plan to combine the CFD absorber model, the experiment on the PNNL LCFS platform, and the Aspen model to better understand the interface area and its influential factors in packed columns. The road map of the DoE is shown in Fig. 4.1.

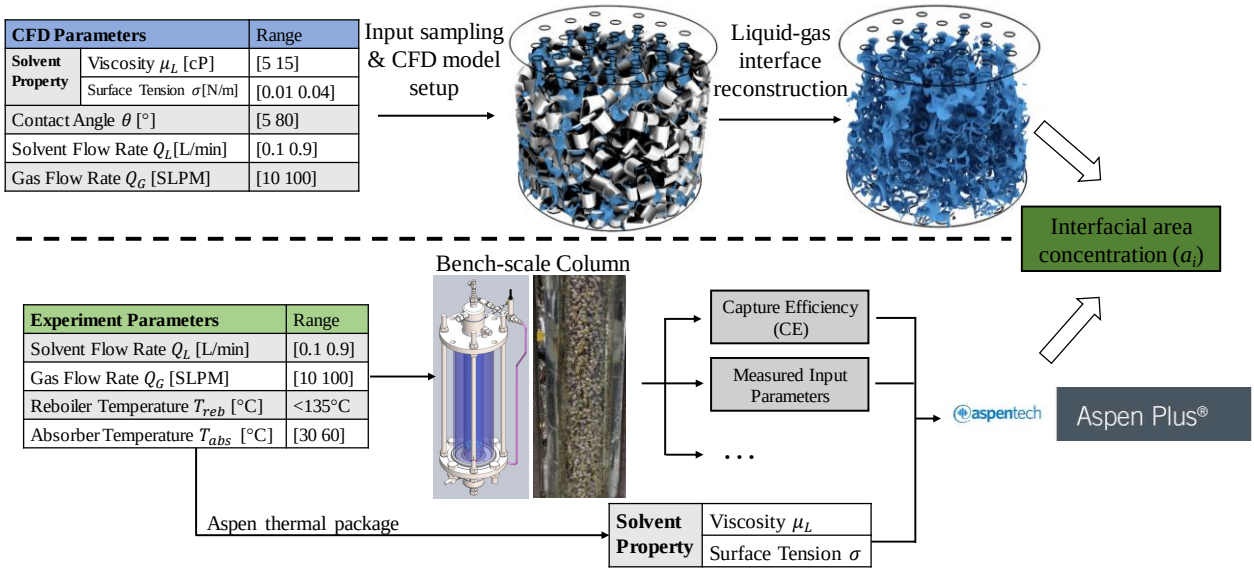

Fig. 4.1 The road map of using the DoE method to connect the experimental data, Aspen model, and CFD simulations for interfacial area prediction.

On the CFD model side, the five input parameters ($u_L, u_G, \theta, \mu_L, \sigma$) are varied independently in the simulation. These ranges cover the operation limits of the LCFS cart and the EEMPA solvent properties. The design of 100 CFD runs is shown in Fig. 4.2. The Latin hypercube sampling method is used to sample each input parameter randomly. With these inputs, the CFD boundary conditions can be determined and the countercurrent flow will be simulated using the RCM filled with Pro-Pak rings. After the simulation reaches a stable condition, the gas-liquid surface will be reconstructed for interfacial area calculation.

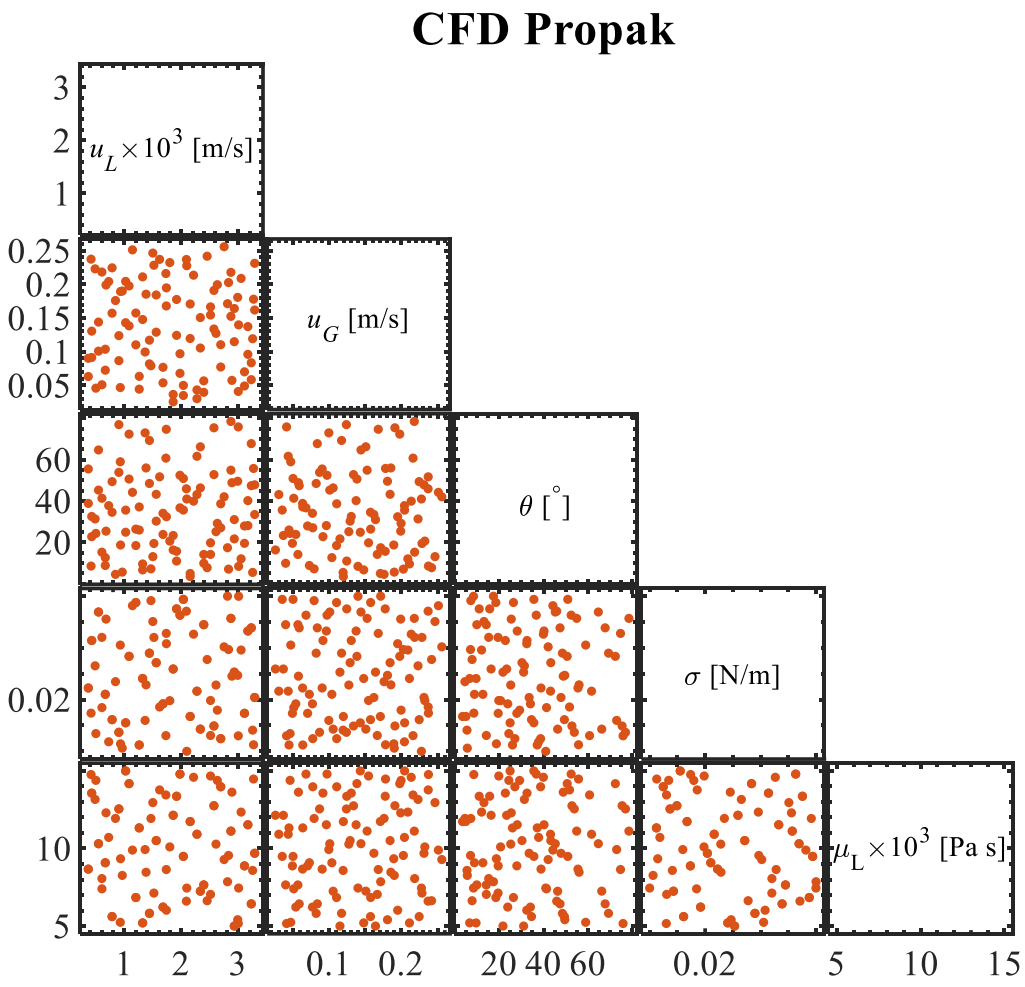

Fig. 4.2 The DoE of inputs for the CFD simulations. Five parameters including liquid flow rate u_L, gas flow rate u_G, contact angle θ, surface tension σ, and viscosity μ_L are selected as the model input.

On the experiment side, with the selected EEMPA solvent, the material properties, such as viscosity μ_L, and surface tension σ, cannot be varied arbitrarily as in CFD simulations. However, by adjusting the reboiler temperature (T_{reb}) and absorber temperature (T_{abs}), it would be possible to affect the interface area and the CO_2 capture efficiency. Along with the direct-controlled solvent flow rate (Q_L) and flue gas flow (Q_G), these four parameters (Q_L, Q_G, T_{reb}, T_{abs}) are identified as the DoE parameters for the experiment. In the experiment, the mass transfer area characterizes the interface between the gas and liquid where the chemical reaction happens for CO_2 capture. The interface area from CFD simulations and experiments can be compared for a better understanding of the mass transfer in a packed column.

To come up with a DoE plan for experiments, the range of the four experiment parameters was first determined based on LCFS operation limits as discussed in Section 3. Based on this information, a 12-run space-filling Latin hypercube design was proposed. The details of the final design are shown in Table 4.1.

Table 4.1 Nominal Experiment Design Plan for LCFS Cart.

Run	Q_L [L/min]	Q_G [SLPM]	T_{reb} [°C]	T_{abs} [°C]
1	0.41	35.0	120	36
2	0.34	25.0	118	48
3	0.31	65.0	116	45
4	0.15	40.0	111	46
5	0.47	60.0	115	37
6	0.44	45.0	104	50
7	0.18	15.0	113	34
8	0.25	50.0	100	39
9	0.22	55.0	107	32
10	0.37	30.0	106	30
11	0.28	10.0	102	43
12	0.50	20.0	109	41

Table 4.2 shows the actual values of the inputs and responses that were subsequently collected for each of the DoE experiments on the LCFS system. In addition to the measured input variables, the measured CO_2 capture fraction is also included. These 12 experiments represent the initial data design for characterization of EEMPA with LCFS. In the experimental process and subsequent data analysis, additional information and considerations have been noted. First, it was reported qualitatively that some experiments may have exceeded the expectations/assumptions of operation in the LCFS experiments, characterized by high SFR/GFR ratio. Experiments 11 and 12 are notably higher in SFR/GFR than other experiments. Second, some experiments may be in an operational regime where the solvent is saturated and therefore CE has low sensitivity to kinetics properties. Data collected under such conditions would provide little information in the calibration of kinetics models. Although this is a consideration for utility in future experiments (and a further DoE design would be cognizant of this, based on the Aspen model's predictions), it does not invalidate the data or analysis using the data.

Table 4.2 Summary of DoE runs on PNNL's LCFS system with Pro-Pak packing.

Run Number	DoE Factors (actual values)						Measured Values			
							Capture Efficiency	Effective Area (m2/m3)		
	Solvent	Packing	L (lpm)	G (slm)	T_reb (°C)	T_abs (°C)		Low	High	Ave
1	EEMPA	ProPak	0.41	35.6	113	42	56%	251	184	218
2	EEMPA	ProPak	0.34	25.6	113	42	59%	257	188	223
3	EEMPA	ProPak	0.30	65.0	111	41	26%	217	140	179
4	EEMPA	ProPak	0.15	40.4	108	37	24%	154	99	126
5	EEMPA	ProPak	0.47	60.2	109	43	35%	231	155	193
6	EEMPA	ProPak	0.43	45.4	105	44	35%	177	130	153
7	EEMPA	ProPak	0.18	15.7	110	35	82%	276	210	243
8	EEMPA	ProPak	0.25	50.2	102	38	31%	190	122	156
9	EEMPA	ProPak	0.22	55.2	107	35	28%	160	109	134
10	EEMPA	ProPak	0.34	30.5	106	39	61%	248	190	219
11	EEMPA	ProPak	0.28	10.2	105	39	93%	405	385	395
12	EEMPA	ProPak	0.49	20.8	107	44	76%	325	261	293

Table 4.3 Summary of DoE runs on CFD RCM with Pro-Pak.

	Operating Conditions				Material Property			
Case	**Solvent Flow Rate**		**Gas Flow Rate**		**Surface Tension**	**Contact Angle**	**Liquid Dynamic Viscosity**	**Interface Area Concentration**
	Q_L [L/min]	**u_L [m/s]**	**Q_G [SLPM]**	**u_G [m/s]**	**σ [N/m]**	**θ [º]**	**μ_L[Pa s]**	**a_i [m^2/m^3]**
1	0.394	0.0014	32.041	0.1171	0.0290	69.3	0.0058	103.1
2	0.884	0.0032	22.857	0.0835	0.0339	67.8	0.0064	145.3
3	0.867	0.0032	37.551	0.1372	0.0333	40.2	0.0115	247.5
4	0.280	0.0010	55.918	0.2044	0.0155	35.6	0.0150	225.0
5	0.182	0.0007	28.367	0.1037	0.0210	12.7	0.0091	331.8
6	0.100	0.0004	24.694	0.0902	0.0223	55.5	0.0087	83.5
7	0.247	0.0009	33.878	0.1238	0.0137	76.9	0.0126	68.2
8	0.541	0.0020	26.531	0.0970	0.0363	52.4	0.0148	172.0
9	0.851	0.0031	19.184	0.0701	0.0174	28.0	0.0089	317.5
10	0.590	0.0022	46.735	0.1708	0.0167	5.0	0.0117	410.0
11	0.524	0.0019	48.571	0.1775	0.0376	15.7	0.0134	396.2
12	0.786	0.0029	59.592	0.2178	0.0357	78.5	0.0111	105.6
13	0.655	0.0024	15.510	0.0567	0.0345	14.2	0.0077	446.9
14	0.149	0.0005	39.388	0.1439	0.0369	64.7	0.0103	92.2
15	0.737	0.0027	30.204	0.1104	0.0125	38.7	0.0140	264.3
16	0.639	0.0023	41.224	0.1507	0.0143	66.2	0.0073	125.0
17	0.557	0.0020	13.673	0.0500	0.0394	50.9	0.0095	163.7
18	0.802	0.0029	44.898	0.1641	0.0253	31.0	0.0050	289.1
19	0.214	0.0008	61.429	0.2245	0.0161	49.4	0.0056	123.4
20	0.361	0.0013	57.755	0.2111	0.0241	9.6	0.0052	405.2
21	0.329	0.0012	43.061	0.1574	0.0388	26.4	0.0068	275.4
22	0.459	0.0017	21.020	0.0768	0.0192	34.1	0.0062	249.4
23	0.508	0.0019	10.000	0.0365	0.0259	23.4	0.0121	331.8
24	0.345	0.0013	17.347	0.0634	0.0112	37.1	0.0113	199.0
25	0.622	0.0023	11.837	0.0433	0.0216	61.6	0.0109	141.7
26	0.704	0.0026	52.245	0.1909	0.0149	75.4	0.0128	126.9
27	0.296	0.0011	54.082	0.1977	0.0284	72.3	0.0142	92.8
28	0.116	0.0004	35.714	0.1305	0.0314	32.6	0.0136	170.0
29	0.900	0.0033	63.265	0.2312	0.0204	47.9	0.0097	188.7
30	0.427	0.0016	50.408	0.1842	0.0271	43.3	0.0105	186.1
31	0.473	0.0017	59.111	0.2160	0.0130	60.7	0.0135	133.3
32	0.373	0.0014	27.223	0.0995	0.0160	72.9	0.0099	83.1
33	0.166	0.0006	13.928	0.0509	0.0185	41.3	0.0074	133.4
34	0.113	0.0004	64.945	0.2374	0.0174	8.6	0.0148	281.0
35	0.255	0.0009	51.807	0.1893	0.0114	18.8	0.0093	278.7
36	0.136	0.0005	12.548	0.0459	0.0134	24.4	0.0144	215.8
37	0.821	0.0030	11.219	0.0410	0.0130	75.8	0.0052	116.1
38	0.688	0.0025	42.264	0.1545	0.0198	19.8	0.0147	392.8
39	0.185	0.0007	54.436	0.1989	0.0356	25.4	0.0123	219.5
40	0.572	0.0021	64.814	0.2369	0.0371	45.9	0.0066	208.9
41	0.895	0.0033	48.686	0.1779	0.0113	55.8	0.0145	209.1
42	0.890	0.0033	32.623	0.1192	0.0141	5.5	0.0086	455.9
43	0.774	0.0028	55.442	0.2026	0.0297	7.1	0.0096	433.6
44	0.714	0.0026	34.802	0.1272	0.0228	25.2	0.0103	332.8
45	0.254	0.0009	12.796	0.0468	0.0305	59.0	0.0052	122.7
46	0.475	0.0017	45.936	0.1679	0.0328	74.7	0.0086	97.3
47	0.415	0.0015	62.485	0.2284	0.0320	19.5	0.0071	330.5
48	0.823	0.0030	38.256	0.1398	0.0400	8.4	0.0074	425.2
49	0.401	0.0015	21.652	0.0791	0.0391	7.2	0.0119	436.0
50	0.791	0.0029	15.715	0.0574	0.0245	48.9	0.0136	195.1
51	0.394	0.0014	22.429	0.0820	0.0290	48.5	0.0058	161.9

Case	Operating Conditions				Material Property			
	Solvent Flow Rate		Gas Flow Rate		Surface Tension	Contact Angle	Liquid Dynamic Viscosity	Interface Area Concentration
	Q_L [L/min]	u_L [m/s]	Q_G [SLPM]	u_G [m/s]	σ [N/m]	θ [º]	μ_L[Pa s]	a_i [m^2/m^3]
52	0.884	0.0032	16.000	0.0585	0.0339	47.4	0.0064	202.4
53	0.818	0.0030	49.429	0.1806	0.0247	49.6	0.0054	181.9
54	0.688	0.0025	45.571	0.1665	0.0131	14.2	0.0070	369.5
55	0.720	0.0026	54.571	0.1994	0.0180	29.2	0.0144	292.8
56	0.867	0.0032	26.286	0.0961	0.0333	28.1	0.0115	324.2
57	0.280	0.0010	39.143	0.1431	0.0155	24.9	0.0150	279.7
58	0.769	0.0028	46.857	0.1712	0.0400	17.4	0.0079	387.8
59	0.378	0.0014	50.714	0.1853	0.0229	56.0	0.0085	128.5
60	0.182	0.0007	19.857	0.0726	0.0210	8.9	0.0091	343.7
61	0.573	0.0021	62.286	0.2276	0.0100	41.0	0.0074	223.8
62	0.100	0.0004	17.286	0.0632	0.0222	38.9	0.0087	153.3
63	0.263	0.0010	52.000	0.1900	0.0106	5.6	0.0083	314.4
64	0.312	0.0011	68.714	0.2511	0.0382	44.2	0.0099	159.9
65	0.492	0.0018	63.571	0.2323	0.0198	20.6	0.0101	340.3
66	0.247	0.0009	23.714	0.0867	0.0137	53.9	0.0126	115.1
67	0.541	0.0020	18.571	0.0679	0.0363	36.7	0.0148	254.0
68	0.753	0.0028	70.000	0.2558	0.0302	42.1	0.0093	216.1
69	0.671	0.0025	66.143	0.2417	0.0278	7.8	0.0066	418.8
70	0.851	0.0031	13.429	0.0491	0.0173	19.6	0.0089	374.6
71	0.590	0.0022	32.714	0.1196	0.0167	3.5	0.0117	429.2
72	0.524	0.0019	34.000	0.1243	0.0376	11.0	0.0134	419.4
73	0.165	0.0006	59.714	0.2182	0.0320	15.3	0.0081	295.9
74	0.786	0.0029	41.714	0.1525	0.0357	54.9	0.0111	173.1
75	0.655	0.0024	10.857	0.0397	0.0345	9.9	0.0077	449.1
76	0.149	0.0005	27.571	0.1008	0.0369	45.3	0.0103	130.2
77	0.737	0.0027	21.143	0.0773	0.0124	27.1	0.0140	335.1
78	0.639	0.0023	28.857	0.1055	0.0143	46.4	0.0072	189.3
79	0.557	0.0020	9.571	0.0350	0.0394	35.6	0.0095	254.4
80	0.802	0.0029	31.429	0.1149	0.0253	21.7	0.0050	355.3
81	0.214	0.0008	43.000	0.1572	0.0161	34.6	0.0056	174.0
82	0.361	0.0013	40.429	0.1478	0.0241	6.7	0.0052	389.3
83	0.606	0.0022	58.429	0.2135	0.0327	39.9	0.0146	227.4
84	0.835	0.0031	57.143	0.2088	0.0296	12.1	0.0123	419.3
85	0.329	0.0012	30.143	0.1102	0.0388	18.5	0.0068	351.4
86	0.459	0.0017	14.714	0.0538	0.0192	23.9	0.0062	313.1
87	0.508	0.0019	7.000	0.0256	0.0259	16.4	0.0121	376.3
88	0.345	0.0013	12.143	0.0444	0.0112	26.0	0.0113	259.7
89	0.622	0.0023	8.286	0.0303	0.0216	43.1	0.0109	202.1
90	0.198	0.0007	55.857	0.2041	0.0118	37.8	0.0107	159.9
91	0.133	0.0005	61.000	0.2229	0.0265	31.4	0.0132	190.3
92	0.704	0.0026	36.571	0.1337	0.0149	52.8	0.0128	177.3
93	0.410	0.0015	67.429	0.2464	0.0351	13.1	0.0130	373.0
94	0.296	0.0011	37.857	0.1384	0.0284	50.6	0.0142	155.3
95	0.443	0.0016	64.857	0.2370	0.0186	51.7	0.0138	169.8
96	0.476	0.0017	53.286	0.1947	0.0308	32.4	0.0060	242.7
97	0.116	0.0004	25.000	0.0914	0.0314	22.8	0.0136	207.3
98	0.900	0.0033	44.286	0.1618	0.0204	33.5	0.0097	272.5
99	0.231	0.0008	48.143	0.1759	0.0235	4.6	0.0119	338.3
100	0.427	0.0016	35.286	0.1290	0.0271	30.3	0.0105	260.5

With 100 CFD data (Table 4.3), a CFD surrogate model using FOQUS [14] was built to predict the corresponding interfacial area at the 12 experimental operation conditions with the Pro-Pak absorber column. The only one unknown parameter contact angle is estimated with a range of 30° to 46°, which is measured by dripping EEMPA solvent droplet on a flat stainless steel surface. The comparisons of these predictions with the actual measurements (translated via Aspen) are shown in the figure below. Here, there is an overall good match between actual and CFD models for all of the tests, except for the two highest capture efficiency values that correspond to the near-equilibrium conditions in the absorber. This region is sensitive to the experimental inputs which result in an unrealistic high a_i in the Aspen prediction.

From the figures, it can be seen that the ranges given by CFD predictions are primarily due to estimated ranges of contact angle for the EEMPA solvent, the variable identified to drive the most uncertainty in the CFD models. To better understand this uncertainty, we need more information on the contact angle of the given solvent and packing in a packed column. A novel method was proposed in the next chapter to combine the CFD models, experiment data, and Aspen model to infer the effective contact angle in the column. More details were provided in the following chapter.

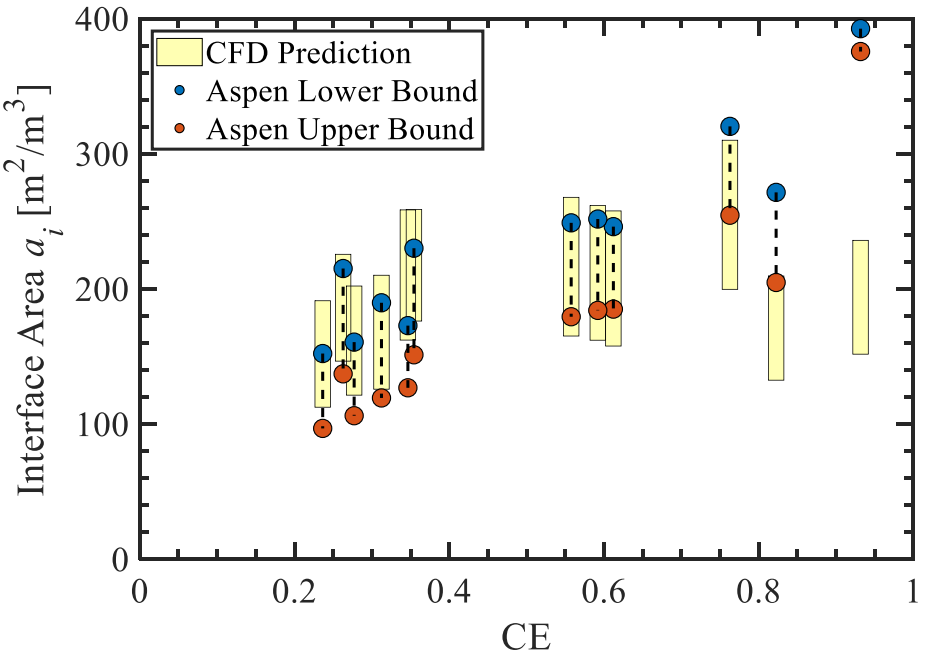

Fig. 4.3 Interfacial area prediction in CFD compared to the actual data processed in AspenPlus from DoE on LCFS system using Pro-Pak and EEMPA solvent.

5 Inference for Contact Angle Using Combined CFD/Aspen/Experiment

Validation and incorporation of CFD modeling in the inferences involves making a connection between EEMPA experimental data, the Aspen model, and the CFD model. Because there are no measurements that directly correspond to the CFD input/output relationship for interfacial area and contact angle, validation proceeded with less direct connections to explore possible validation paths. The goal was formulated to use CFD in a chain of inference to correspond contact angle to experimentally observed results.

Knowing contact angle for a given experimental configuration would provide one facet of a means to estimate the relative efficiency of a complex packing, allowing a better correspondence between the performance of absorbers in model and experiment. By utilizing corresponding information gained from experiments, Aspen models, and CFD models, there is a potential path to making a connection between measurable physical conditions and contact angle.

Table 5.1 describes the notations used in this chapter. Underlined variables indicate explicitly uncertain parameters (i.e., those quantities are statistical distributions).

Table 5.1 Notations used in this chapter.

Notation	**Parameter**
CA	Contact Angle
I_A	Interfacial Area
I_A-Aspen	Interfacial Area associated with Aspen model
I_A-CFD	Interfacial Area associated with CFD model
ST	Surface Tension
V	Viscosity
T_A	Absorber Temperature
SFR	Solvent Flow Rate
GFR	Gas Flow Rate
$\underline{\theta}$	Aspen Model Uncertain Parameters
CE	Capture Efficiency

5.1 CFD Model and Inverse Analysis for CA

The CFD model's behavior is a correlation:

$$I_A = f\left(ST,V,SFR,GFR,CA\right). \tag{3.12}$$

We can extract and use this correlation by running the model at various settings of five independent variables, getting I_A for each run. This relationship is easily captured with a simple parametric response surface, providing access to the CFD-based relationship in these quantities.

The response surface was created as a quadratic regression equation, including all first-order terms (i.e., SFR, GFR), first-order interactions (i.e., SFR*GFR, SFR*ST), and second-order terms (i.e., SFR^2, GFR^2). This describes the full quadratic model. Through backward model selection, a reduced model was found that performs just as well as the full model.

In the full model, we tested each coefficient for significance and removed those that failed, starting with higher-order terms. Of the squared terms, ST^2, CA^2, and V^2 all failed individual significance testing and, when comparing models including and not including these terms, no significant difference existed. Thus, these three terms were removed. A similar operation was performed with the next factors with low significance: SFR*ST, GFR*ST, SFR*V, GFR*V, CA*V were removed.

Now we have our final response surface model, as all other coefficients are highly significant. Details of this process are in Table 5.2.

Table 5.2 Factors in the CFD response surface emulator.

Model	Terms Included	R-squared	Adjusted R-squared
Full Quadratic	SFR, GFR, ST, CA, V, SFR*GFR, SFR*ST, SFR*CA, SFR*V, GFR*ST, GFR*CA, GFR*V, ST*CA, ST*V, CA*V, SFR^2, GFR^2, ST^2, CA^2, V^2	0.9882	0.9801
Reduced	SFR, GFR, ST, CA, V, SFR*GFR, SFR*ST, SFR*CA, SFR*V, GFR*ST, GFR*CA, GFR*V, ST*CA, ST*V, CA*V, SFR^2, GFR^2	0.9862	0.9789
Final	SFR, GFR, ST, CA, V, SFR*GFR, SFR*CA, GFR*CA, ST*CA, ST*V, SFR^2, GFR^2	0.9829	0.9773

Once the final model was found, some analysis regarding the behavior of the model was conducted. It became clear that of all the inputs, CA had the strongest relationship with I_A. However, as noted during the model selection process, all inputs contribute significantly to the overall relationship with I_A and together describe over 98% of the variation we see in I_A.

Table 5.3 displays the coefficients for each term in the response surface along with an indicator for its significance. Four different symbols are used to indicate the p-value as: *** = p-value < 0.01; ** = p-value in [0.01, 0.05); * = p-value in [0.05, 0.1); . = p-value ≥ 0.1. The terms are separated by order (first-order, first-order interaction, second-order).

Table 5.3 CFD response surface emulator coefficients and significance.

Term	Coefficient	
CA	$-3.021 * 10^{-3}$	***
SFR	$2.550 * 10^{-1}$	***
V	3.366	*
ST	1.310	*
GFR	$2.819 * 10^{-4}$	.

Term	Coefficient	
GFR*CA	$1.502 * 10^{-5}$	***
ST*CA	$-2.676 * 10^{-2}$	***
SFR*CA	$8.151 * 10^{-4}$	**
ST*V	$-1.488 * 10^{2}$	*
SFR*GFR	$-5.908 * 10^{-4}$	*

Term	Coefficient	
SFR^2	$-1.874 * 10^{-1}$	***
GFR^2	$-7.958 * 10^{-6}$	***

Given this CFD emulator in regression form, inverse analysis is straightforward. The interest here is in the value of CA given the other parameters (CA | {ST, V, SFR, GFR, I_A}). This can be thought of as the stochastic function:

$$\underline{CA} = g\left(ST, V, SFR, GFR, I_A\right). \tag{3.13}$$

Although this inverse problem is straightforward, $\underline{CA}$ is always a distribution because of emulator uncertainty.

It is noted that since the analysis was performed, a revision of CFD was made, and runs re-run. The following analysis and conclusion are derived based on the CFD data before revision. However, the developed procedures would be applicable for analyzing the revised CFD data.

5.2 LCFS Physical Experiments

LCFS experiments measure actual capture efficiency. This can be thought of as getting the information from a function:

$$\mathrm{CE}=\mathrm{h}\left(\mathrm{SFR},\ \mathrm{GFR},\ \mathrm{T_A}\right). \tag{3.14}$$

Twelve experiments were performed. The description of the experiments and data has been discussed in Section 4. This information was reported previously, but some additional comments were added regarding the potential consistency of underlying science across all the runs and features of the LCFS data.This is only a subset of the information in the relationships required by the CFD-based correlation in *f* and *g*. To make the link, an Aspen model is introduced.

5.3 Aspen Model of Physical Experiments and Interfacial Area

Details of the Aspen modeling, previously reported, are in Appendix A. Aspen modeling of the LCFS has this relationship:

$$CE,\ I_A - Aspen = k\ (SFR,\ GFR,\ T_A,\ ST,\ V, \Theta), \tag{3.15}$$

$$\Theta = [\beta_{IA1}\ \beta_{MT1}\ k_{10}\ k_{20}\ E_A]. \tag{3.16}$$

The parameters described in Appendix A (β_{IA1} for the interfacial area, β_{MT} for mass transfer, and k_{10}, k_{20}, and E_A for reaction kinetics) are determined through inverse analysis. This has been documented previously, and an overview is given in Appendix A.

The formulation of the inverse analysis problem for the Aspen model parameters is:

$$\Theta = inverse\left(k \mid CE,\ T_A,\ GFR,\ SFR,\ ST,\ V\right). \tag{3.17}$$

First, the Aspen model is calibrated to get distributions for the parameters (Θ) for the CO_2BOLS solvent under study. The viscosity is calculated as a function of temperature and composition using a correlation developed from the available viscosity data and incorporated into the Aspen model as a Fortran subroutine. The surface tension, however, is represented by a built-in model (Onsager-Samaras model for mixture surface tension of electrolytes) available in Aspen, since no data are available for developing a more accurate model. In the established Bayesian model calibration framework, the approach is to build and validate an emulator based on a number of Aspen models runs, specify prior distributions (ranges) for

the parameters, and solve for the posterior distributions of those parameters that allow the model to best match data. Here, the data is the 12 LCFS experiments. An emulator was constructed and validated, and the posterior distributions of the parameters in the set Θ were sampled (as a non-closed-form inverse problem, these distributions are represented by a large number of samples drawn with MCMC).

Now, we have a stochastic function in principle:

$$CE = h\left(SFR,\ GFR,\ T_A\right). \tag{3.18}$$

Given the distributions for the parameters in Θ and the LCFS data, we can forward propagate the uncertain parameters to find an I_A for each data point as shown in equation below. And the 12 experiment run I_A prediction results are shown in Fig. 5.1.

$$I_A - Aspen = m\left(SFR,\ GFR,\ T_A,\ ST,\ V,\ \Theta\right). \tag{3.19}$$

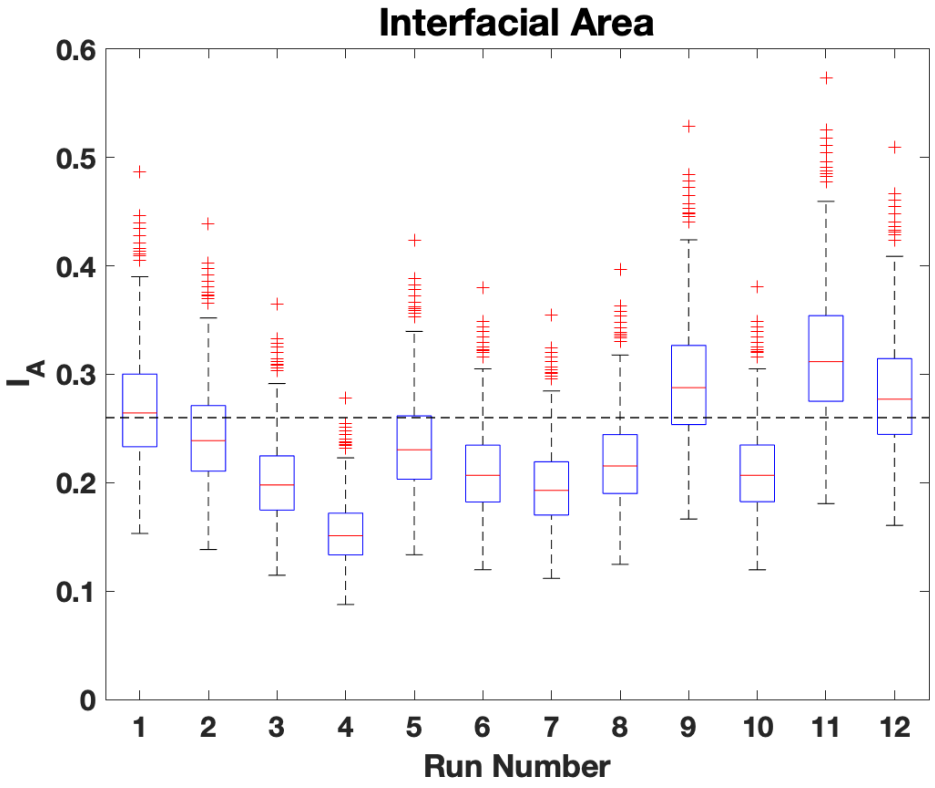

Fig. 5.1 I_A-Aspen inferred distributions corresponding to each LCFS experiment. Distributions are sampled, and the samples are presented here in standard box plot format. The dashed line is the maximum value of IA-CFD found in any of the simulations run across the inclusive ranges of inputs.

5.4 Results: Inference of Contact Angle

Above, we described the ability in principle, to extract specific values relating:

$$CA = g\ (ST,\ V,\ SFR,\ GFR,\ T_A, I_A - Aspen) \tag{3.20}$$

for each LCFS experiment.

For a given LCFS experiment *i*, settings (ST, V, SFR, GFR, T_A)$_i$ are known. We can then abbreviate this as:

$$CA = g_i(I_A - Aspen)\,. \tag{3.21}$$

As described above, this function g_i is an inverse problem based on the emulator of the CFD response. The inverse analysis is described in Fig. 5.2: starting with the function g_i, shown in panel (a), the predicted I_A-Aspen (panel [b]) corresponds to the plotted y-axis of the function and is used to infer a contact angle as in panel (c).

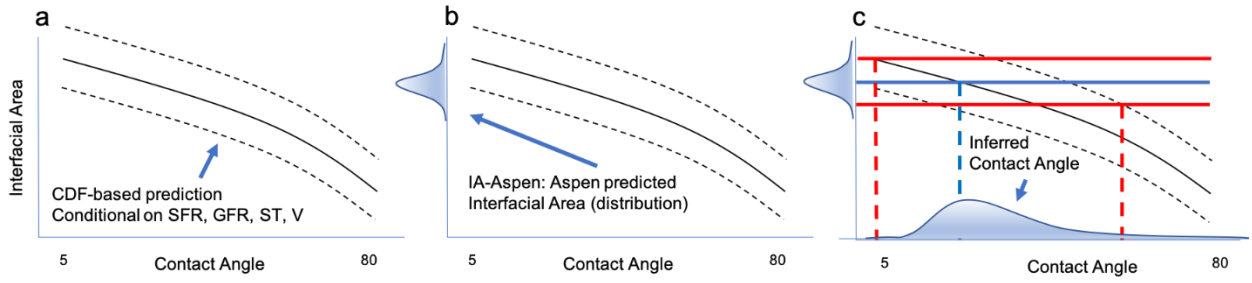

Fig. 5.2 Conceptual process for inferring contact angle given interfacial area: (a) Based on CFD simulations, the relationship between contact angle and the interfacial area is known, with emulator uncertainty, given values of solvent flow rate, gas flow rate, surface tension, and viscosity, corresponding to an instance of LCFS experimental settings; (b) interfacial area predicted by Aspen from the same experiment is a distribution propagated from calibrated parameter uncertainty; (c) contact angle distribution is the result of the inverse analysis.

Actual analysis for LCFS Experimental Run 4 is shown in Fig. 5.3. For this example, the analysis shows potential, despite the lack of correspondence of some of the right tail of the I_A-Aspen distribution.

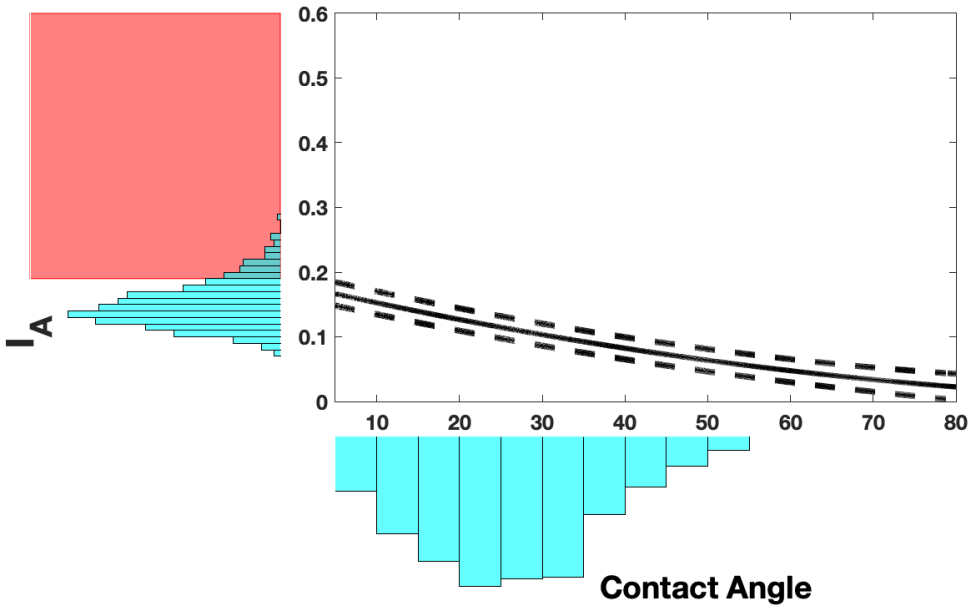

Fig. 5.3 Contact angle inference for LCFS Experiment 4. The red box indicates the tail of the I_A-Aspen distribution that does not correspond to a contact angle.

The problem with the tail in Experiment 4 is far more of an issue in Experiment 9, where the inference process is shown in Fig. 5.4. In this case, it is clear that there are fundamental issues with the correspondence, and it is not possible to perform the inverse projection of Fig. 5.2 to attain a distribution in contact angle.

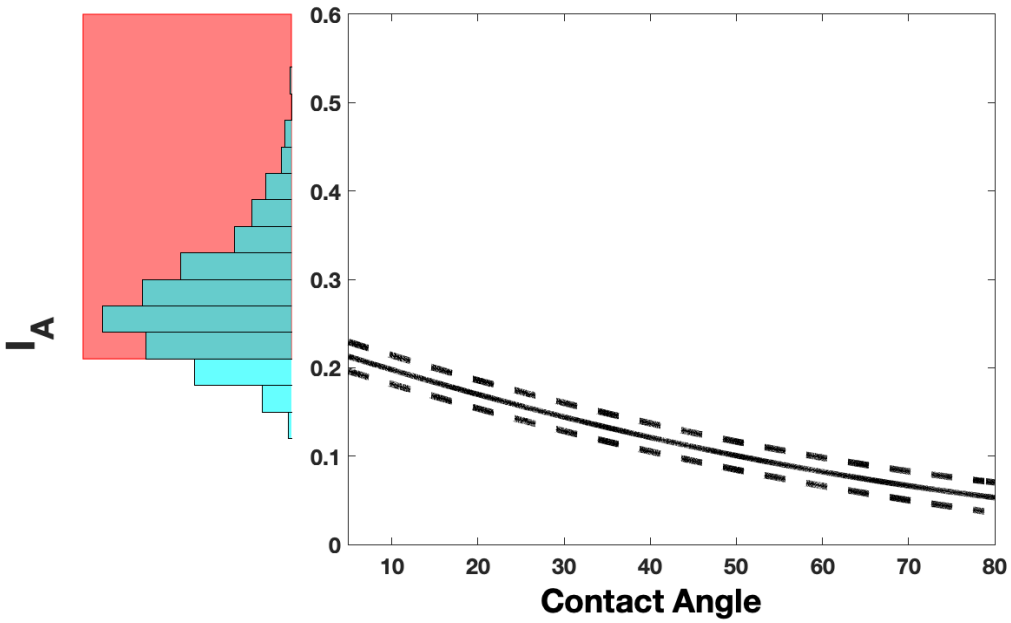

Fig. 5.4 Contact Angle inference correspondence for LCFS Experiment 9. The red box indicates the part of the I_A-Aspen distribution that does not correspond to a contact angle.

In fact, the result is that the I_A-CFD and I_A-Aspen are indistinct and only partly overlapping ranges in general. Fig. 5.5 shows all of the components of the inference for each LCFS experiment: the black curve of the CFD-derived CA vs. I_A conditional on the values that the LCFS experiment was run, and the I_A-Aspen inferred distribution (in this figure, mean and confidence intervals, rather than the full distributions) also corresponding to that particular LCFS experiment.

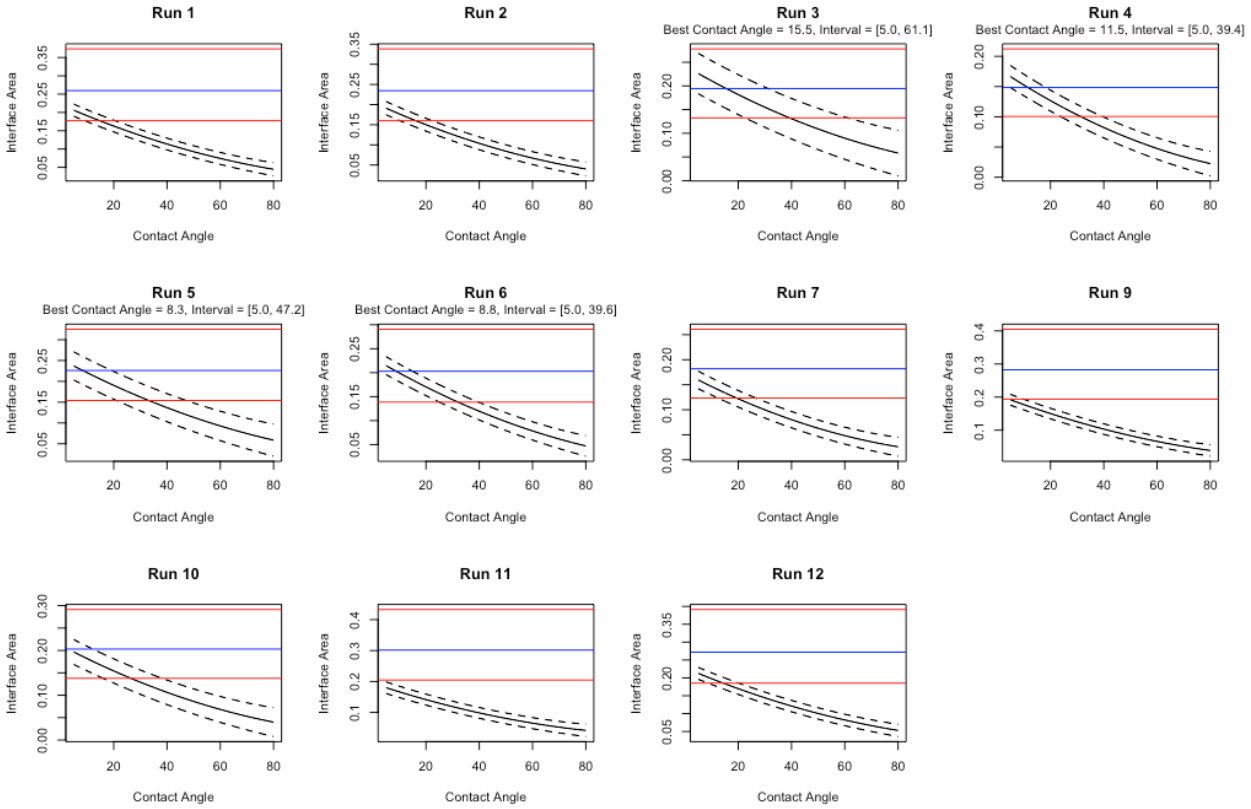

Fig. 5.5 Contact Angle inference diagrams for all LCFS experiments. For compact presentation, the mean and 95% confidence interval of the I_A-Aspen distributions are shown projected horizontally from the y-axis.

5.5 Discussion

Several assumptions were made in order to be able to complete this analysis that connects the Aspen and CFD results. Perhaps the most crucial one being that the Aspen model's definition of I_A can reasonably be interpreted as the same quantity as the CFD model's I_A. At project inception, we recognized that this was a potential issue and initially had called the results from the CFD "Interfacial Area" and the results from the Aspen model "Effective Area" to acknowledge potential differences in definition and interpretation. For the purpose of scientific study and to be able to proceed with the analysis, this correspondence was provisionally accepted to see what progress could be made.

The process for using the Aspen and CFD models in conjunction to provide indirect validation of the models has been established in principle, and the elements of the work and connection between the stages are sound. In the end, the results from the 12 runs give mixed conclusions. For a few of the runs, there looks

to be reasonable agreement between the I_A values from the two models that make it to draw conclusions about plausible ranges of the CA. For other runs, there is limited to no agreement between the I_A values from the Aspen and CFD models. Based on these inconsistent results and the lack of direct measurement of I_A and CA, we are forced to reserve judgement about how the validation process should be interpreted. Because of this disconnect, there is, at best, only indirect information to be used for the CFD validation. This issue should be a topic of further discussion if more direct validation and greater confidence in the conclusion is desired.

If investment were to be made to further enhance the validation process, the following ideas may merit consideration: (1) Currently, the CFD and Aspen models do not use the same set of inputs for a given experimental run. Some of the required inputs for the CFD model rely on being able to estimate those quantities using the Aspen model. If the inputs could be directly matched, it would be easier to interpret results. (2) The CFD model currently does not incorporate possible changes across the different heights in the column, but rather reports an average quantity for several aspects that are known to change throughout the system. Updating the CFD in its next generation to incorporate this complexity would add realism and make results more interpretable. (3) The current Aspen model requires a value of contact angle to be provided for estimation. Because of lack of access to some of the proprietary components of the model, this contact angle was effectively set to 0 to generate results. The circuitous logic of assuming a value of CA, to then generate an I_A value to compare to the CFD model to estimate CA is undesirable and would be helpful to remedy in future generations of the models.

6 Conclusion

In summary, absorber CFD column models were first developed at two differente levels with different focus. A DoE plan was designed with ~100 CFD runs carried out on the PNNL high performace clusters and ~12 experiments carried out on PNNL's LCFS platform. A novel method was proposed to combine the CFD simulations, the column experiment results, and the Aspen models together to provide better understanding of the interface area in packed column. Since the contact angle was identified as the single strongest influencing factor on the interface area from the sensitivity study, preliminary study was carried out to infer more information on the effective contact angles in packed column.

1. The proposed CFD model can simulate the random packing process and generate a realistic pattern of packing elements in packed column. A composite particle model is proposed in the DEM process for packing generation. The composite particle model can be designed to simulate various packing elements. The generated Raschig ring, Pro-Pak, and Pall ring packing are verified with the packings in the experimental packed column. A correct absorber column porosity and specific area can be achieved by the proposed composite particle model.

2. The full-size laboratory-scale CFD model can correctly demonstrate the wall and entrance effects on the simulated countercurrent flow hydrodynamics. It has the capability of modeling the effect of solvent distributor on the solvent distribution in the packed column, compared to the design without the distributor.

3. The CFD model with 100 runs from DoE design covers a wide range of column operation conditions and solvent properties, which can affect the interface area and CO_2 capture efficiency in a packed column. The sensitivity study of 100 CFD runs demonstrates that the contact angle exihbits the largest influence on the interface area in packed column, followed by the solvent flow rate and surface tension. The solvent viscosity has minimuim effects, which is consistant with the observation from University of Texas [12], [15], [16].

4. Column experiments were carried out on the PNNL LCFS platform with capture fraction data collected for ~12 runs with varying operating conditions from DoE deisgn. The Aspen model was used first to estimate the interface area based on the capture fraction. The CFD prediction of the interface area was compared with the Aspen prediction to infer the effective contact angles in the column with given solvents and packings.

Appendix A. Aspen Model Details

This information was reported previously and is included here for reference.

The PNNL DOCCSS team provided their Aspen model of the CO_2BOL solvent and associated process. This model was adapted by the CCSI[2] team to include an interfacial area correlation, rather than to treat the interfacial area as constant. The interfacial area correlation selected below followed the work in (Ataki, 2006), and was implemented in the Aspen model through use of a Fortran subroutine.

$$\frac{a_h}{a} = \beta_{IA1} Fr_L^{\beta_{IA2}} We_L^{\beta_{IA3}} Re_L^{\beta_{IA4}} (\cos\theta)^{\beta_{IA5}} \quad \text{(A.1)}$$

In Eq. A.1, $\frac{a_h}{a}$ represents the interfacial area fraction in the packing. The liquid-phase Froude, Weber, and Reynolds numbers are represented as Fr_L, We_L, and Re_L, respectively. The contact angle is given by θ. The model parameters are represented as β_{IAi}, and the chosen settings are presented in Table A.1.

Table A.1 Deterministic settings for interfacial area model parameters.

Parameter	Value
β_{IA1}	Uncertain
β_{IA2}	0.197
β_{IA3}	-0.136
β_{IA4}	0.043
β_{IA5}	0

The parameters (β_{IA2}, β_{IA3}, β_{IA4}) associated with the contributions of dimensionless groups are fixed at the values in Table A.1, which were specified in Ataki (2006)[17]; this choice was made due to the limited amount of data available for parameter estimation in the interfacial area model. Since contact angle is not directly treated as a variable in the rate-based column model available in Aspen, its value is fixed in the model and the value of β_{IA5} is fixed to zero in order to mute the effect of the contact angle in the calculation of the interfacial area model. As more data become available, parameters β_{IA2}, β_{IA3}, and β_{IA4} may be more rigorously estimated in order to more precisely quantify the effect of individual dimensionless groups on the interfacial area. Further work may also include the development of a correlation for contact angle as a function of solvent physical properties and process operating conditions, which will allow for its effect to be included in the interfacial area correlation.

The liquid-phase mass transfer coefficient (k_L) is modeled as:

$$k_L = \beta_{MT_1} k'_L \tag{A.2}$$

In Eq. A.2, k'_L refers to the mass transfer as calculated in the work of Mathias et al. (2015)[18], based on a modified version of the Onda correlation, and β_{MT_1} is a fitting parameter used for adjusting the model for the EEMPA solvent system.

The reactions for the system are assumed to be:

$$2DIAM + CO_2 \leftrightarrow DIAMH^+ + DIAMCOO^- \tag{A.3}$$

$$DIAM + CO_2 + H_2O \leftrightarrow DIAMH_2^+ + HCO_3^- \tag{A.4}$$

In these reaction equations, $DIAM$ refers to the EEMPA solvent species, $DIAMH^+$ and $DIAMH_2^+$ its protonated forms, and $DIAMCOO^-$ its carbamate form. The reaction rate equations are assumed to be analogous to those presented in Mathias et al. (2015)[18].

An absorber-stage model (only) was used for the purposes of this analysis, and reboiler temperature was removed as an input. The reason for this was to simplify focus on the interfacial area correlation within the absorber column without varying the lean loading of the solvent. This allows for an initial analysis to see what effects the flow regimes and temperatures have on the interfacial area and, ultimately, on the capture percentage of the absorber column. Capture percentage was the primary output metric, and the experimental input space explored as inputs used are solvent flow rate, gas flow rate, and absorber temperature.

In order to maximize the value of the bench scale runs, five key Aspen model parameters were identified for the UQ analysis: interfacial area coefficient (I_A Coef—referred to as β_{IA1} in Eq.A.1); kinetic pre-exponential factors for the two reactions (*k10* and *k20*); the activation energy, which was assumed to be the same for both the of the reactions (following Mathias et al. 2015[18]); and a mass transfer coefficient (MT1—referred to as β_{MT_1} in Eq. A.2).

Appendix B. Aspen Model Calibration and Posterior Distributions

This information was reported previously and is included here for reference.

Established Bayesian calibration techniques (Kennedy and O'Hagan, 2001[19]) were used to calibrate the CO_2BOL-based Aspen model. These approaches have previously been successful for several sorbent and solvent-based systems within the CCSI^2 project (e.g., Russell et al., 2020[20]). The method begins with the specification of a set of prior distributions on the relevant parameters (above). A likelihood function is specified to quantify the comparison of a relevant output metric from model to experiment, here the comparison of Aspen to the LCFS data, in capture percentage. Parameter prior expectations are updated to posterior distributions that make the simulation model consistent with the capture percentage observations, as defined by the statistical model. Details of the approach are available in the references above.

A statistical surrogate for the Aspen model was developed, as a tool to enable the sampling required to generate posterior distributions on parameters. The Aspen surrogate was verified to be accurate using a cross-validation study of 50 test runs, resulting in a model vs. prediction R2=0.9917.

The Aspen model (as summarized by the surrogate) was compared to the 12 experimental runs (with capture percentage as the metric) using Bayesian model calibration to obtain an estimate of the Aspen process model parameter distributions with respect to the experimental outcomes. The updated posterior distribution of the five Aspen model parameters based on the information from the 12 experimental runs are shown in Fig. B.1.

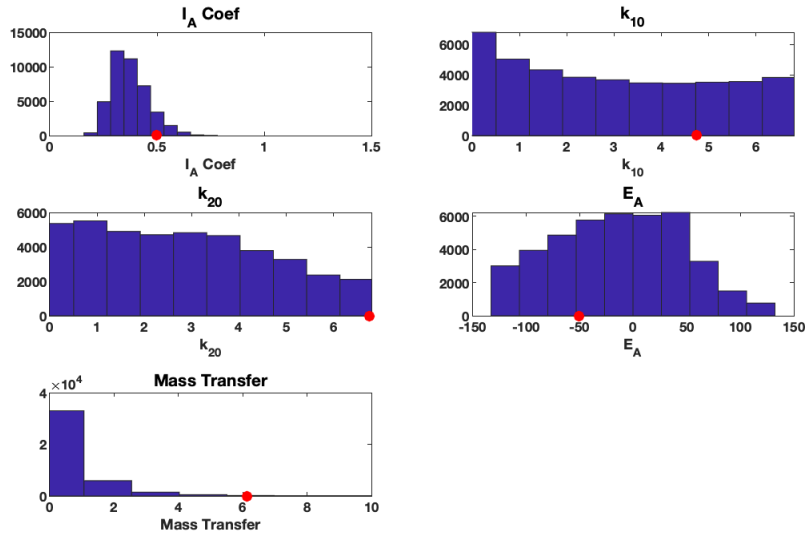

Fig. B.1 Posterior distribution of selected National Energy Technology Laboratory/Los Alamos National Laboratory Aspen model parameters. The red marker shows default values.

7 Reference

[1] "CD-adapco STAR-CCM+ 13.04 User Guide." 2018.

[2] C. . Hirt and B. . Nichols, "Volume of fluid (VOF) method for the dynamics of free boundaries," *J. Comput. Phys.*, vol. 39, no. 1, pp. 201–225, Jan. 1981.

[3] J. U. Brackbill and D. B. Kothe, "ScienceDirect - Journal of Computational Physics : A continuum method for modeling surface tension*1," *J. Comput. Phys.*, vol. 335354, 1992.

[4] S. Muzaferija and M. Perić, "Computation of free surface flows using interface-tracking and interface- capturing methods," *Nonlinear Water Wave Interact.*, pp. 59–100, 1999.

[5] Z. Chen, D. Yates, J. K. Neathery, and K. Liu, "The effect of fly ash on fluid dynamics of CO 2 scrubber in coal-fired power plant," *Chem. Eng. Res. Des.*, vol. 90, no. 3, pp. 328–335, 2012.

[6] P. A. Cundall and O. Strack, "A discrete numerical model for granular assemblies," *Geeotechnique*, vol. 29, no. 29, pp. 47–65, 1979.

[7] C. Lillie and P. Wriggers, "Three-dimensional modelling of discrete particles by superellipsoids," vol. 102, no. December 2006, pp. 101–102, 2016.

[8] B. Nassauer, T. Liedke, and M. Kuna, "Polyhedral particles for the discrete element method: Geometry representation, contact detection and particle generation," *Granul. Matter*, vol. 15, no. 1, pp. 85–93, 2013.

[9] T. Zhao, F. Dai, N. W. Xu, Y. Liu, and Y. Xu, "A composite particle model for non-spherical particles in DEM simulations," *Granul. Matter*, vol. 17, no. 6, pp. 763–774, 2015.

[10] Yeom, Ha, Kim, Jeong, Hwang, and Choi, "Application of the Discrete Element Method for Manufacturing Process Simulation in the Pharmaceutical Industry," *Pharmaceutics*, vol. 11, no. 8, p. 414, Aug. 2019.

[11] Y. Fu, J. Bao, R. Singh, C. Wang, and Z. Xu, "Investigation of Countercurrent Flow Profile and Liquid Holdup in Random Packed Column with Local CFD Data," *Chem. Eng. Sci.*, p. 115693, Apr. 2020.

[12] R. Tsai, "Mass Transfer Area of Structured Packing," The University of Texas at Austin, 2010.

[13] D. Song, A. F. Seibert, and G. T. Rochelle, "Mass Transfer Parameters for Packings: Effect of Viscosity," *Ind. Eng. Chem. Res.*, vol. 57, no. 2, pp. 718–729, 2018.

[14] D. C. Miller *et al.*, "Innovative computational tools and models for the design, optimization and control of carbon capture processes," in *Computer Aided Chemical Engineering*, vol. 38, Elsevier, 2016, pp. 2391–2396.

[15] D. Song, A. F. Seibert, and G. T. Rochelle, "Effect of Liquid Viscosity on Mass Transfer Area and Liquid Film Mass Transfer Coefficient for GT-OPTIMPAK 250Y," *Energy Procedia*, vol. 114, pp. 2713–2727, 2017.

[16] C. Wang, "Mass transfer coefficients and effective area of packing," University of Texas at Austin, 2015.

[17] A. Ataki, "Wetting of Structured Packing Elements - CFD and Experiment," Technische Universität Kaiserslautern, 2006.

[18] P. M. Mathias *et al.*, "Measuring the Absorption Rate of CO2 in Nonaqueous CO2-Binding Organic Liquid Solvents with a Wetted-Wall Apparatus," *ChemSusChem*, vol. 8, no. 21, pp. 3617–3625, 2015.

[19] M. C. Kennedy and A. O'Hagan, "Bayesian calibration of computer models," *J. R. Stat. Soc. Ser. B, Stat. Methodol.*, vol. 63, no. 3, pp. 425–464, 2001.

[20] C. S. Russell *et al.*, "Improving full-scale models of new carbon capture technologies with uncertainty quantification," *Environ. Div. 2018 - Core Program. Area 2018 AIChE Annu. Meet.*, pp. 56–65, 2018.